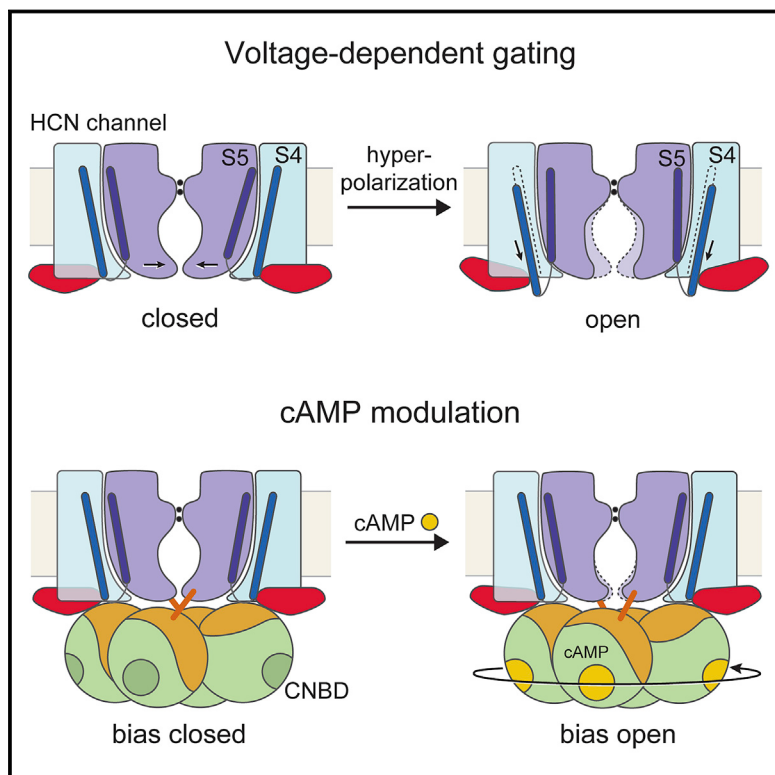


Structures of the Human HCN1 Hyperpolarization-Activated Channel

Graphical Abstract



Authors

Chia-Hsueh Lee, Roderick MacKinnon

Correspondence

mackinn@rockefeller.edu

In Brief

Cryo-EM structures of the human HCN1 hyperpolarization-activated ion channel provide mechanistic insights on voltage-dependent gating with reversed polarity.

Highlights

- Structures of the human HCN1 hyperpolarization-activated channel at 3.5 Å resolution
- Channel filter adopts a unique conformation, allowing both K⁺ and Na⁺ to permeate
- Long S4 helix and unusual coupling to the pore mediate reversed polarity gating
- Cyclic AMP induces a rotation of cytoplasmic domains to favor channel opening

Structures of the Human HCN1 Hyperpolarization-Activated Channel

Chia-Hsueh Lee¹ and Roderick MacKinnon^{1,2,*}

¹Laboratory of Molecular Neurobiology and Biophysics, The Rockefeller University, Howard Hughes Medical Institute, 1230 York Avenue, New York, NY 10065, USA

²Lead Contact

*Correspondence: mackinn@rockefeller.edu
<http://dx.doi.org/10.1016/j.cell.2016.12.023>

SUMMARY

Hyperpolarization-activated cyclic nucleotide-gated (HCN) channels underlie the control of rhythmic activity in cardiac and neuronal pacemaker cells. In HCN, the polarity of voltage dependence is uniquely reversed. Intracellular cyclic adenosine monophosphate (cAMP) levels tune the voltage response, enabling sympathetic nerve stimulation to increase the heart rate. We present cryo-electron microscopy structures of the human HCN channel in the absence and presence of cAMP at 3.5 Å resolution. HCN channels contain a K⁺ channel selectivity filter-forming sequence from which the amino acids create a unique structure that explains Na⁺ and K⁺ permeability. The voltage sensor adopts a depolarized conformation, and the pore is closed. An S4 helix of unprecedented length extends into the cytoplasm, contacts the C-linker, and twists the inner helical gate shut. cAMP binding rotates cytoplasmic domains to favor opening of the inner helical gate. These structures advance understanding of ion selectivity, reversed polarity gating, and cAMP regulation in HCN channels.

INTRODUCTION

Rhythmic cycles, such as spontaneous and repetitive firing patterns in excitable cells, are essential timing mechanisms that regulate various biological processes. Not unexpectedly, the pacemaker current (also known as funny current I_f or hyperpolarization-activated current I_h) was first described in the heart (Brown et al., 1979), the most reliable rhythmic organ of the body. Later also characterized in nerves (Mayer and Westbrook, 1983), this current was found to be mediated by hyperpolarization-activated cyclic nucleotide-gated (HCN) ion channels (Gauss et al., 1998; Ludwig et al., 1998; Santoro et al., 1998). HCN channels contribute to cardiac and neuronal pacemaker activity. In sinoatrial node cells, these channels account for the initial phase of the action potential and, hence, regulate the firing rate. HCN channels are modulated by intracellular cyclic nucleotides (DiFrancesco and Tortora, 1991), including cyclic adenosine monophosphate (cAMP). The activity of channels is

augmented in the presence of cAMP, and such facilitation is crucial to accelerating the heart rate under sympathetic stimulation (Brown et al., 1979; DiFrancesco and Tortora, 1991). In the nervous system, widely expressed HCN channels are involved in neuronal excitability and network activity (Benarroch, 2013). Given their multiple roles, dysfunction of HCN channels has been implicated in a spectrum of diseases (DiFrancesco and DiFrancesco, 2015; Verkerk and Wilders, 2015)—for instance, arrhythmias, epilepsies, and neuropathic pain—making HCN channels attractive new targets for therapeutic exploration (Postea and Biel, 2011; Tibbs et al., 2016). One HCN channel blocker, ivabradine, was recently approved for clinical use to treat chronic heart failure (Tibbs et al., 2016).

HCN channels belong to the superfamily of six-transmembrane segment channels, and are related to cyclic nucleotide-gated (CNG) channels and voltage-dependent K⁺ (K_v) channels K_v10–K_v12. In addition to their physiological significance, intriguing biophysical properties of HCN channels motivate us to observe their molecular architecture. First, the HCN channel, despite having a selectivity filter sequence that contains all of the essential amino acids required for K⁺ selectivity, allows both K⁺ and Na⁺ to pass through its pore, yielding a reversal potential of -20 to -30 mV under physiological conditions (Gauss et al., 1998; Ludwig et al., 1998; Santoro et al., 1998). Thus, when the HCN channel opens, cations flow into the cell and cause depolarization, in contrast to K⁺ channels, whose opening generally repolarizes the cell. Second, the polarity of voltage-dependent gating is reversed in HCN channels compared to most other voltage-dependent ion channels: depolarization causes closure, and hyperpolarization causes opening. Finally, the open probability of HCN can be increased by cAMP, but unlike CNG channels, cyclic nucleotides are not a prerequisite for channel opening. To understand the molecular basis of ion selectivity, reversed polarity, gating and cAMP modulation, we determined structures of the human HCN channel in the ligand-free and cAMP-bound states using single-particle cryo-electron microscopy (cryo-EM).

RESULTS AND DISCUSSION

HCN1 Channel Architecture

We determined structures of the human HCN1 channel expressed without its C terminus to improve its stability in detergent (Figure S1). The truncated channel, HCN1_{EM}, is activated by membrane hyperpolarization, is cation permeable like the full-length channel, and is sensitive to cAMP (Figures S2A–S2D).

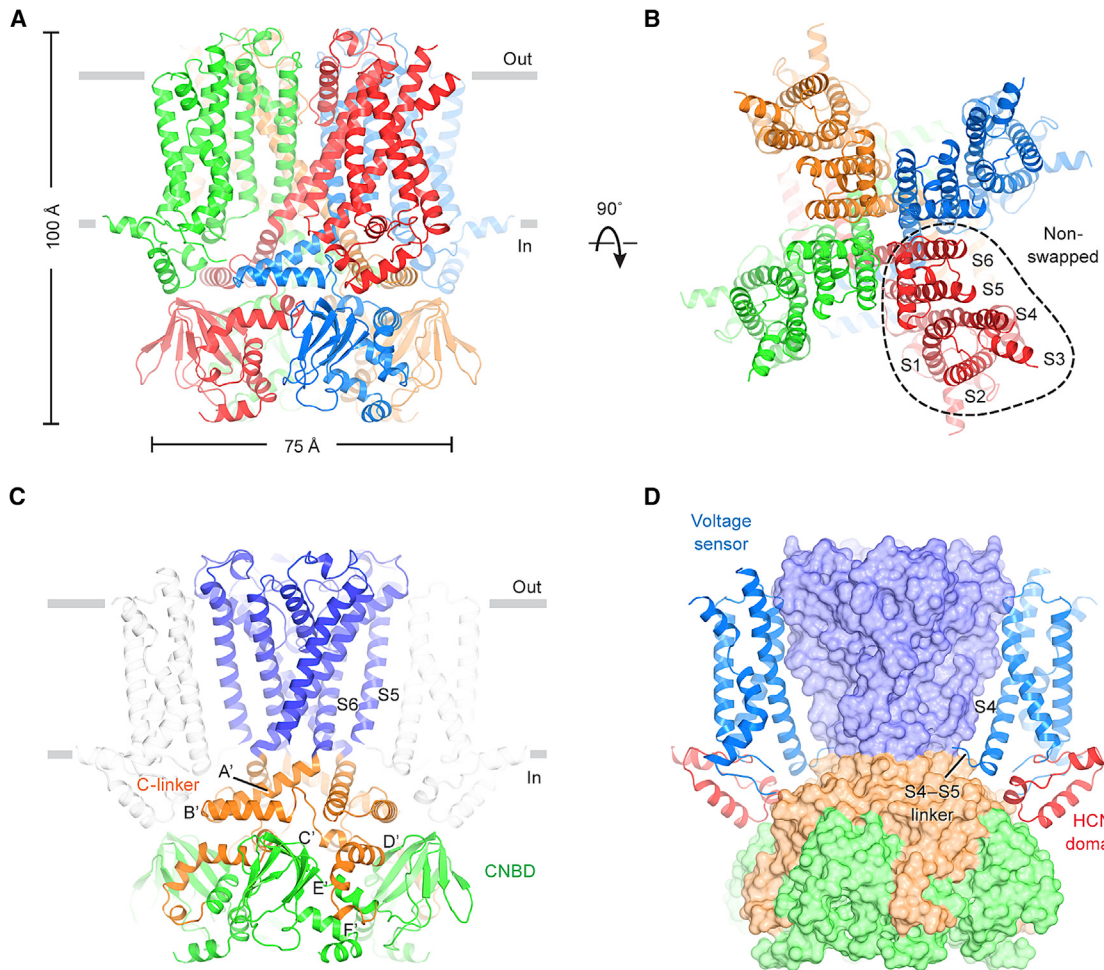


Figure 1. Architecture of the Human HCN1 Channel

(A and B) Structure of the channel tetramer in the ligand-free state, viewed parallel to the membrane (A) or from the extracellular side (B). Each subunit is shown in a different color. Gray bars represent approximate boundaries of the membrane bilayer. (C and D) Domain organization of the HCN channel. In (C), the pore domain (helices S5 and S6) is colored blue, the C-linker disk (A'- and B'-helices) and four following helices (C'- to F'-helices) are colored orange, and the CNBD is colored green. In (D), the voltage sensors and the HCN domains are shown as ribbons, whereas the pore and C-terminal domains are in surface representation. The voltage sensor from the subunit nearest to the viewer is removed for clarity. See also Figures S1, S2, S3, and S5.

Reconstructions of HCN1_{EM} in the ligand-free and cAMP-bound states were carried out to an overall resolution of 3.5 Å (Figures S3 and S4; Table S1). Nearly complete atomic models for the structured core of the protein were built (Figures S1 and S5). Density for N-terminal residues 1–93 was not visible because these residues are most likely unstructured and disordered (nearly 30% are glycines). The refined models correlate well with the density maps and have good stereochemistry (Table S1). While significant conformational changes were observed in the cytoplasmic domains, the ligand-free and cAMP-bound structures are similar in the transmembrane domains (root mean square deviation [RMSD] of C α = 0.43 Å). We will describe the ligand-free structure first and then discuss conformational changes induced by cAMP binding.

The HCN channel is ~100 Å in length perpendicular to the membrane and ~75 Å in width when viewed from within the

plane of the membrane (Figures 1A and 1B). Four identical subunits form a 4-fold symmetric pore (helices S5 through S6), which is surrounded by membrane-embedded voltage sensors (helices S1 through S4), as in K_v channels. The voltage sensors in HCN1 are “non-swapped,” which means each voltage sensor contacts the pore through amino acids from the same polypeptide chain (i.e., same subunit), as depicted in Figure 1B. In contrast, based on known molecular structures and a structure-based analysis of K_v channel amino acid sequences (Whicher and MacKinnon, 2016), in K_v1–K_v9 and voltage-dependent Na⁺ and Ca²⁺ channels, the voltage sensors interact with an adjacent subunit (i.e., they are domain swapped). The domain-swapped voltage sensors permit a long α -helical S4–S5 linker, which likely functions as a mechanical lever through which voltage-sensor conformational changes impart force to open or close the pore’s gate (Long et al., 2005, 2007). In HCN1, the S4–S5 linker is much

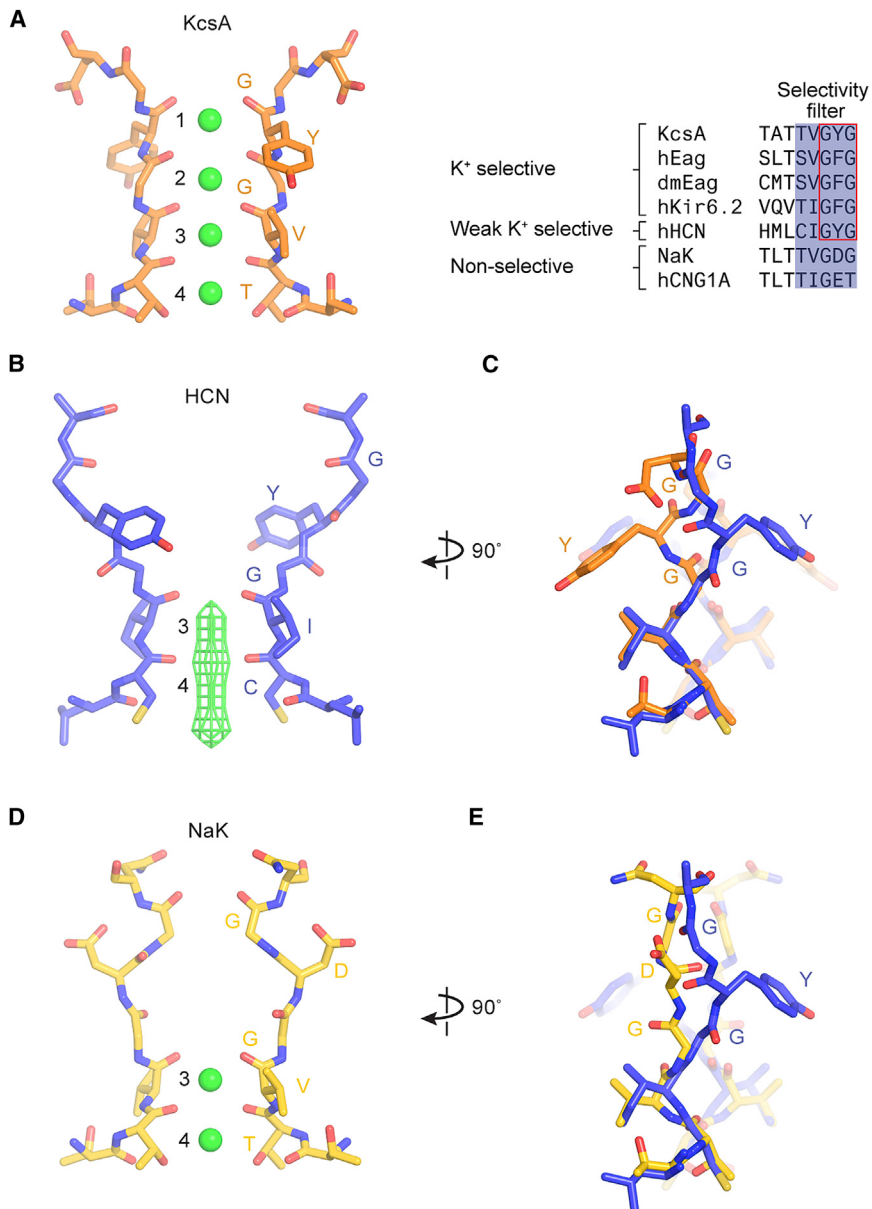


Figure 2. Selectivity Filter of the HCN1 Channel

(A) Structure of the KcsA filter, a K⁺-selective filter (PDB: 1K4C). Discrete K⁺ binding sites (1 to 4) are labeled. K⁺ ions within the filter are represented as green spheres. A sequence alignment of the filter regions from selected channels is shown on the right.

(B) Structure of the HCN1 filter, a weak K⁺-selective filter. The density of K⁺ ions is represented as green mesh. The map is sharpened with a b-factor of -120 Å² and contoured at 5.5 σ.

(C) Comparison of the HCN1 and KcsA filters. The superposition of the HCN (blue) and KcsA filters (orange) is based on Cα atoms of residues 357 to 359 of the HCN channel. K⁺ ions in the KcsA channel are removed for clarity.

(D) Structure of the NaK filter, a non-selective filter (PDB: 2AHZ).

(E) Comparison of the HCN1 and NaK filters. See also Figure S6.

shorter and not α-helical (Figure 1D). In the absence of an α-helical lever, non-swapped voltage sensors must apparently work in a different manner to regulate the gate.

The pore-lining S6 inner helices form a right-handed, tightly packed bundle within the membrane's inner leaflet (Figure 1C). At the level of the intracellular membrane-water interface, the S6 helices make a sharp bend and give rise to a helix-turn-helix "C-linker," which forms an α-helical disk just below the membrane. C-terminal to the C-linker, the polypeptide chain then gives rise to five additional short α helices (C'- to F'- and A-helices) and a β-jelly roll that is characteristic of cyclic nucleotide binding domains (CNBDs) (Figures 1C and S1) (Lolicato et al., 2011; Zagotta et al., 2003). Four CNBDs—one from each subunit—are docked onto the cytoplasmic face of the C-linker

disk (Figure 1C). As we describe later, cAMP binding to the CNBD induces conformational changes to affect gating.

The HCN channel exhibits an additional unique feature that may also contribute to this channel's very unusual gating. The 45 amino acids preceding S1 form a 3-α-helical domain that is wedged between the voltage sensor and the cytoplasmic domains (Figure 1D). As far as we can tell, this domain is unique to HCN channels, and therefore, we call it the HCN domain. It contacts the S4 helix (near the short S4-S5 linker) from the same subunit and the C-linker and CNBD from an adjacent subunit. In the context of the tetramer, the HCN domains appear like pincers that constrict the channel at the level of the C-linker disk.

The Selectivity Filter

HCN channels are non-selective monovalent cation channels, permitting K⁺ over Na⁺ by a ratio ~4:1 (Gauss et al., 1998; Ludwig et al., 1998; Santoro et al., 1998), not very different from NaK and hCNG1A channels, which permit K⁺ over Na⁺ by a ratio of 1:1 (Derebe et al., 2011; Kaupp et al., 1989). In comparison, K⁺ channels select K⁺ over Na⁺ by a ratio greater than 1000:1 (Neyton and Miller, 1988; Yellen, 1984). This difference in selectivity is especially notable when one considers that HCN channels actually contain the essential amino acids that are required to form the K⁺ selectivity filter. In the K⁺ channel, protein atoms from the sequence (T/S)XG(Y/F)G directly coordinate K⁺ ions (Figure 2A), and furthermore, the first residue (T/S) is mutable to C (the residue present in HCN) without alteration of selectivity (Zhou and MacKinnon, 2004). Therefore, we ask, why is this close relative of the K⁺ channel non-selective? This deviation

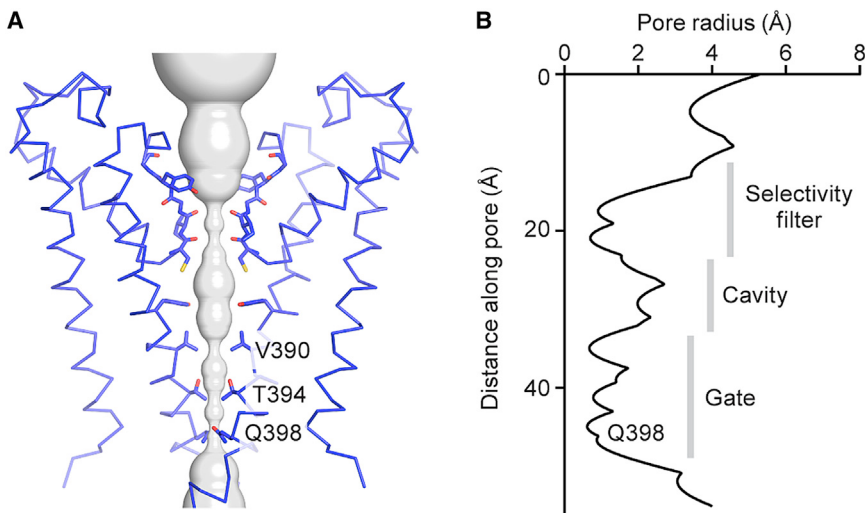


Figure 3. Pore of the HCN1 Channel

(A) Ion pore with only two subunits shown, viewed from within the membrane. The minimal radial distance from the center axis to the protein surface is colored in gray. Selected residues facing the pore are in stick representation, and constricting residues are labeled.

(B) Radius of the pore. The van der Waals radius is plotted against the distance along the pore axis.

from K⁺ selectivity is key to its function as a membrane-depolarizing channel.

Potassium selectivity comes from the precise geometry of the selectivity filter, in which K⁺ ions are coordinated by protein oxygen atoms (Figure 2A). Four ion binding sites, 1–4, exist within the filter (Figure 2A) (Zhou et al., 2001). When selectivity filters from distantly related K⁺ channels are compared, deviations in structure are so small that estimates are limited by measurement error, which, in the best case, is less than 0.2 Å, underscoring the importance of the K⁺ filter's specific geometry (Nishida et al., 2007). In contrast, the selectivity filter in HCN is strikingly different than in the K⁺ channel (Figures 2B and S6A), with an RMSD of 2.9 Å for C_α atoms. In HCN, the Tyr side chain in the GYG sequence is reoriented almost 180 degrees compared to the Tyr in the K⁺ selectivity filter (Figure 2C). The main chain carbonyl oxygen atoms, which ordinarily would form sites 1 and 2, are no longer directed toward the ion pathway in HCN (Figures 2B and 2C). Consequently, HCN preserves only K⁺ binding sites 3 and 4. The outer half of the selectivity filter in HCN is dilated and sites 1 and 2 are absent.

The conformational difference between HCN and the K⁺ selectivity filter is likely due to changes in surrounding amino acids that interact with the filter. For example, the Tyr side chain in the GYG sequence in many K⁺ channels interacts with specific amino acids on the pore helix (i.e., Trp68 and Thr72 in the KcsA K⁺ channel) that form hydrogen bonds with the Tyr hydroxyl (Figure S6B) (Doyle et al., 1998; Shealy et al., 2003; Zhou et al., 2001). In HCN, the Trp and Thr on the pore helix are replaced by Lys and His (Figure S6B), respectively, thus offering a possible explanation for reorientation of the filter Tyr.

The observation that only sites 3 and 4 are maintained in HCN explains its non-selectivity. The multi-ion nature of the K⁺ selectivity filter (four sites allow 2 K⁺ ions to bind simultaneously) is essential to K⁺ selectivity for the following reason: a filter in which only a single ion can bind, even if the binding is thermodynamically favorable for K⁺ over Na⁺, will not exhibit strong kinetic selectivity because an entering Na⁺ ion, which will only reside very briefly, will rapidly exit to either side (i.e., it can permeate).

Multi-K⁺-ion occupancy will increase the probability that a Na⁺ will exit from the same side it entered (because there is a K⁺ ion blocking the other side) and thus permit kinetic selectivity. This behavior has been demonstrated through elegant experiments in the NaK channel (Derebe et al., 2011; Lockless, 2015; Shi et al., 2006), which also has only sites 3 and 4

in its selectivity filter (Figure 2D). The structure of the NaK filter is clearly different than the filter in HCN (Figures 2D and 2E), but the two channels have in common only two monovalent cation binding sites.

Voltage Sensor Control of the Pore

The other intriguing question is HCN's reversed polarity of voltage-dependence, the structural basis of which has never been observed. Most voltage-dependent ion channels open when the membrane is depolarized. HCN channels respond to voltage in the opposite manner, closing with depolarization and opening with hyperpolarization (Gauss et al., 1998; Ludwig et al., 1998; Santoro et al., 1998). But puzzlingly, in most obvious respects, the amino acid sequence of HCN channels would seem to be similar to other voltage-dependent K⁺ channels. What can the structures tell us about voltage dependence with reversed polarity?

The gate of HCN1 is closed by a tightly packed inner helical bundle that constricts the pore to a radius of about 1 Å at amino acid positions Val390, Thr394, and Gln398 (Figures 3A and 3B). In fact, the inner helices are so tightly packed that the volume of the central cavity in the HCN channel is much smaller than in the KcsA channel (Doyle et al., 1998). Concomitantly, the voltage sensors are in a depolarized conformation (Figures 4A and 4B). This conclusion is based on a direct comparison of the HCN1 voltage sensor with that of the K_v1.2–2.1 paddle chimera (Figures 4C and 4D), whose voltage sensor is known to be in a depolarized conformation (Long et al., 2007; Tao et al., 2010). S4 helix positions labeled R0–R4 are located on the extracellular side of the gating charge transfer center (Figure 4B, green and red residues; Figure S6C), as in the depolarized K_v1.2–2.1 voltage sensor. A depolarized voltage sensor conformation, together with a closed pore, corresponds to the expected physiological state of an HCN channel at 0 mV (Figure S2). How do these voltage sensor and pore conformations fit together into a coherent mechanistic scheme, and how might the voltage sensor allow the pore to open when the membrane is hyperpolarized?

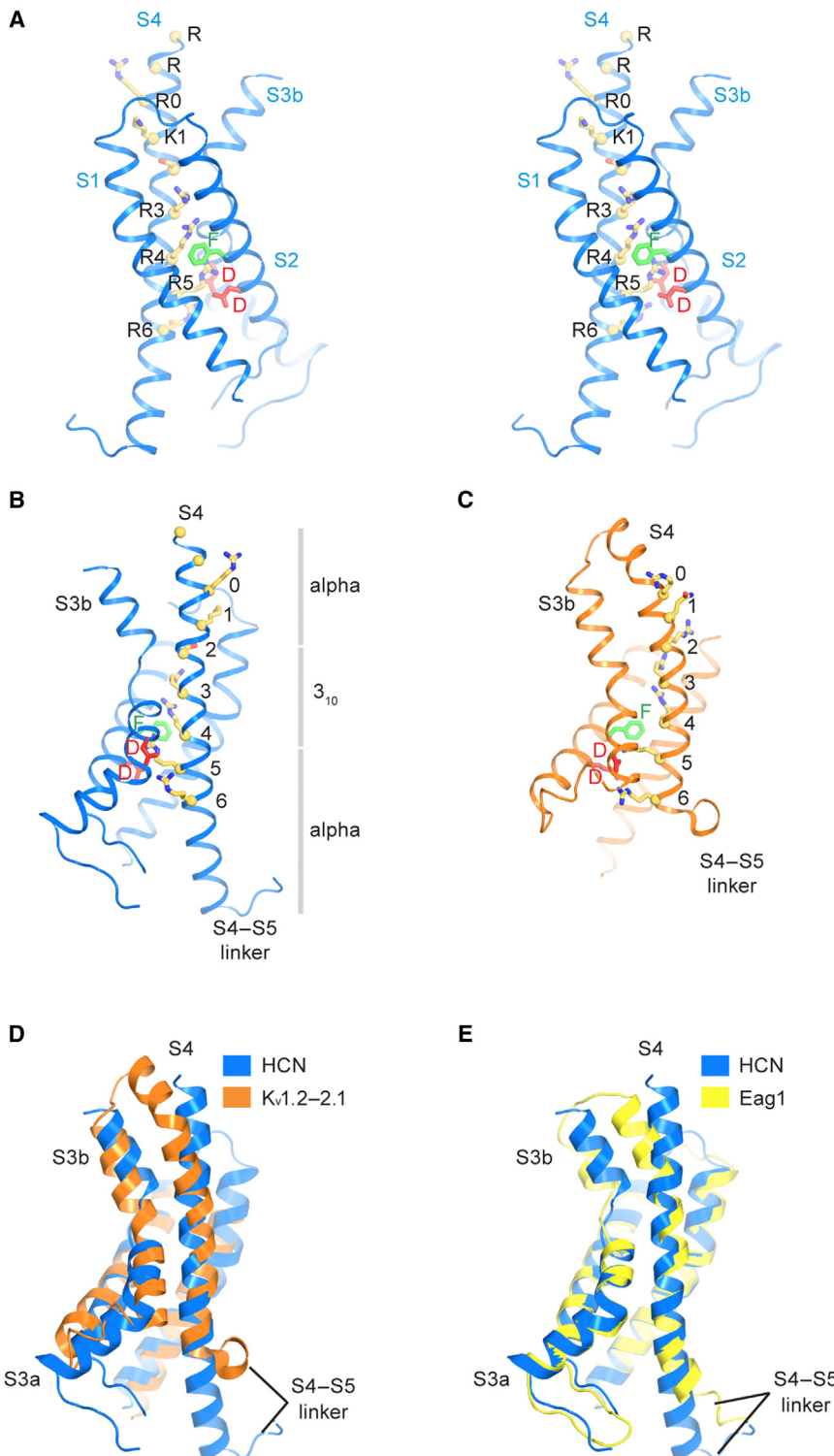


Figure 4. Voltage Sensor of the HCN1 Channel

(A) Stereo view of the voltage sensor. Yellow spheres denote $\text{C}\alpha$ positions of Arg252, Arg255, Arg258 (R0), Lys261 (K1), Ser264, Arg267 (R3), Arg270 (R4), Arg273 (R5), and Arg276 (R6). Residues that form the gating charge transfer center are labeled (Phe186, green; Asp189 and Asp225, red).

(B and C) Comparison of the HCN1 and $\text{K}_v1.2-2.1$ voltage sensors (PDB: 2R9R). The gray bars in (B) show the extents of α - versus 3_{10} -helical transitions in the S4 helix of the HCN1 channel.

(D) Superposition of the HCN1 and $\text{K}_v1.2-2.1$ voltage sensors using $\text{C}\alpha$ atoms of S1 and S2 helices. The S1-S2 loop of $\text{K}_v1.2-2.1$ is not shown for clarity.

(E) Superposition of the HCN1 and Eag1 voltage sensors (PDB: 5K7L), using $\text{C}\alpha$ atoms of S1 to S3 helices.

See also Figure S6.

the membrane electric field (Aggarwal and MacKinnon, 1996; Seoh et al., 1996). Compared with other voltage-dependent channels, the S4 helix of HCN1 contains two additional helical turns on the cytoplasmic side (Figures 4D and 4E). Consequently, it extends further than the S1–S3 helices, beyond the membrane surface into the cytoplasm. The extension of S4 in HCN1 brings the S4–S5 linker into contact with the C-linker of a neighboring subunit (Figure 5A). Force exerted by S4 in this position onto the C-linker has the correct orientation to twist the C-linker disk in a direction that will wrap the right-handed helical bundle formed by the S6 helices, which form the pore's gate, closed. This contact can be made in the depolarized conformation of the voltage sensor only because the S4 is so long. We propose that this is one of the features of the HCN channel that allows it to stabilize a closed pore when the voltage sensor is depolarized. In keeping with this hypothesis, in the Eag1 ($\text{K}_v10.1$) channel, which is related to HCN but opens with depolarization, the S4, because it is shorter (Figure 4E), does not extend into the cytoplasm and does not contact the C-linker in its depolarized conformation (Whicher and MacKinnon, 2016). In fact, we suggest that, in Eag1, when the membrane is hyperpolarized, its S4–S5 linker will move into the cytoplasm to make contacts with the C-linker that are similar to those observed here in HCN1 in the depolarized conformation.

We observe another aspect of HCN's architecture that may also support pore closure upon depolarization. Helices S6, S5,

The unique feature of the HCN1 voltage sensor, which we believe accounts for its reversed polarity, is the extraordinary length of its S4 helix (Figure 4A). The S4 helix is the structural element that contains positive-charged amino acids for sensing

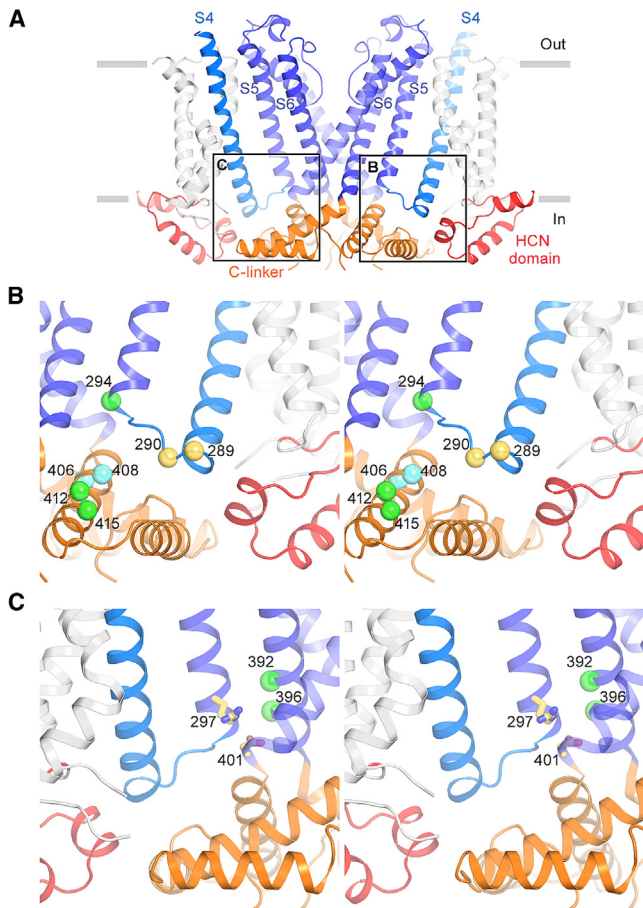


Figure 5. Coupling between the Voltage Sensor and Pore

(A) Interactions between the voltage sensor, pore, and cytoplasmic domains. S1 to S5 helices from the subunits nearest and farthest to the viewer are removed for clarity. The boxes indicate approximate regions of the views shown in (B) and (C).

(B) Stereo view of interactions between the S4–S5 linker, S5 helix, and C-linker. Residues 289 and 290 that may interact with the HCN domain are shown as yellow spheres. Residues on the C-linker that “lock-open” the channel when cross-linked with residue 294 are represented as green spheres. Residues on the C-linker that “lock-close” the channel when cross-linked with residue 294 are represented as cyan spheres.

(C) Stereo view of interactions between S4, S5, and S6 helices. The salt bridge forming residues, Arg297 and Asp401, are shown as yellow sticks. Residues that “lock-open” the channel after Cd²⁺ crosslinking are represented as green spheres.

See also Figure S6.

and S4 are in close contact with each other, almost in a plane (Figures 5A and S6D). S5 and S6 are so well-packed that amino acid side chains interlock like the elements of a zipper (Figure S6D). S4, while not as near, directly contacts S5 for almost its entire length. In addition, in the cytoplasm, the HCN domain appears to buttress this plane of three helices and force the intracellular end of S4 in toward the pore axis (Figures 5A–5C), while it also contacts the outer edge of the C-linker disk. These features of the structure raise the possibility that lateral contacts from the voltage sensors and HCN domains compress the pore so that it is held closed.

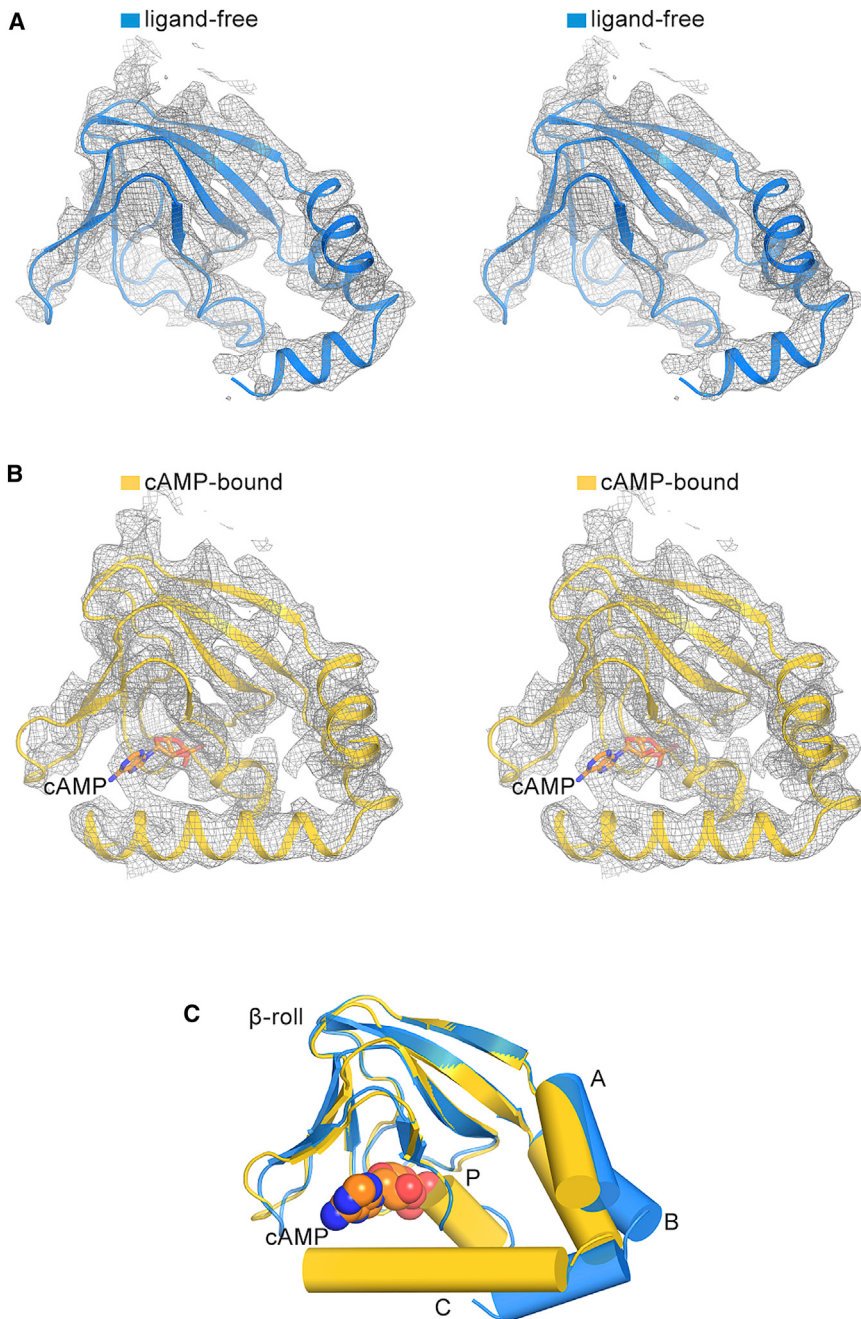
The structural features described above lead us to hypothesize that the closed pore is stabilized by the voltage sensors and HCN domains in the depolarized conformation. If we add to this proposal a conjecture that the S6 helices (which form the gate) are in a higher energy conformation when closed (i.e., they would open if unbiased by the voltage sensor and S5), then a plausible model for HCN voltage-dependent gating is as follows: S4 helix displacement, driven by hyperpolarization, would release the constraints on the C-linker and S6 imposed by S4, allowing the pore to open.

This hypothesis is supported by numerous functional studies in which mutational perturbations and cross-links have been used to probe the activity of HCN channels. Mutations on the S4–S5 linker (Tyr289 and Asp290) cause HCN to open with less negative hyperpolarizing voltages (Chen et al., 2001a). This fits with the idea that the S4–S5 linker serves to hold the pore closed and that these mutations interfere with this function (Figure 5B). Similarly, mutations involving Arg297 and Asp401 also favor channel opening (Decher et al., 2004; Nava et al., 2014). These amino acids form a salt bridge between S5 and S6 helices (Figure 5C), appearing therefore to stabilize the closed channel. A series of lock-open and lock-closed Cd²⁺-mediated cross links by Yellen and colleagues also lend support to the proposed model of gating (Kwan et al., 2012; Rothberg et al., 2003). Cd²⁺ reaction with Cys residues at positions 392 and 396 on the S6 helix (from the same but not adjacent subunit) “lock-open” the pore (Figure 5C, green spheres). These positions lie on the face of S6 contacting S5, buried at the interface in the closed conformation. If, upon hyperpolarization, S5 is pulled by S4 away from S6 and Cd²⁺ then reacts, it would presumably destabilize the closed channel by preventing the S5 helix from again adopting its packed-against-S6 closed-channel conformation. Cross bridges between positions 294 at the bottom of S5 and positions 412 or 415 on the C-linker also lock the channel open (Figure 5B, green spheres). This is also consistent with the idea that S5 is pulled out and down by S4. In this case, rotation of the C-linker disk associated with gate opening (due to unwrapping of the right-handed bundle of S6 helices) would bring the C-linker residues in close contact with the down-displaced bottom of S5. Concordantly, cross links between the same position 294 and 406 or 408, which occur just C-terminal to the bend where S6 gives rise to the C-linker (Figure 5B, green and cyan spheres), lock HCN in a closed conformation.

It has been shown that a truncation mutation devoid of the C-linker and cyclic nucleotide binding domains still retains hyperpolarization-activated gating (Wainger et al., 2001). It thus appears that, in this mutant, the forces on S6 imposed by S4 and S5 are alone sufficient to gate the channel.

Cyclic Nucleotide Modulation

In addition to membrane voltage, the gating of HCN channels is also influenced by cyclic nucleotides. Intracellular cAMP binds to CNBDs, accelerates activation kinetics, and shifts the activation curve to more positive voltages (DiFrancesco and Tortora, 1991; Gauss et al., 1998; Ludwig et al., 1998; Santoro et al., 1998). To understand the mechanism of cAMP modulation, we determined the structure of HCN1 in the presence of cAMP. The quality of the



density map is sufficient to identify the ligand and associated protein conformational changes (Figures 6 and S4F). The overall structure of the cAMP-bound CNBD is similar to that described in crystal structures of isolated domains (Figure S7), and cAMP binds at a location consistent with previous studies (Figure 6B) (Chen et al., 2001b; Lolicato et al., 2011; Zagotta et al., 2003). Local superposition of the ligand-free and cAMP-bound CNBDs (using the β-jelly rolls) shows the conformational changes near the binding pocket that are induced by cAMP (Figure 6C). Specifically, binding of cAMP stabilizes the P-helix and causes the A-, B-, and C-helices to approach the β-jelly roll, as has been

Figure 6. Cyclic AMP-Induced Conformational Changes in the CNBD

(A) Stereo view of CNBD density in the absence of cAMP. The density map (gray mesh) is sharpened with a b-factor of -90 \AA^2 and contoured at 6.5σ . (B) Stereo view of CNBD density in the presence of cAMP. The density map (gray mesh) is sharpened with a b-factor of -120 \AA^2 and contoured at 6.5σ . The cAMP is represented as sticks with carbon atoms in orange, oxygen in red, and nitrogen in blue. (C) Superposition of CNBDs in the ligand-free (blue) and cAMP-bound states (yellow) based on Cα atoms of the β-jelly roll. A-, B-, C-, and P-helices are shown in cylinders, and cAMP is shown in spheres.

See also Figures S4 and S7.

suggested based on both spectroscopic and crystallographic studies of isolated domains (Goldschen-Ohm et al., 2016; Puljung et al., 2014; Saponaro et al., 2014). In addition, helices D and E, not observed in the ligand-free cryo-EM structure, become ordered in the cAMP-bound state (compare Figures 7A and 1C). These helices may play a role in the binding and action of TRIP8b, a protein that regulates HCN trafficking and gating (DeBerg et al., 2015; Santoro et al., 2009; Saponaro et al., 2014; Zolles et al., 2009).

Prior studies using isolated domains (without transmembrane regions), although valuable, provide limited structural information on how cAMP binding modulates the ion channel pore. Here, global superposition (using the pore helices) of two complete channel structures shows how the local conformational changes within the CNBDs propagate to the pore via the C-linkers (Figures 7B–7D). As can be seen in the stereo image (Figure 7B), the displacement of S6 is small, consistent with the fact that cAMP binding alone in the absence of a hyperpolarizing membrane voltage is insufficient to open the channel (Gauss et al., 1998; Ludwig et al., 1998; Santoro et al., 1998). It is

noteworthy, however, that the C-linker rotation and S6 helix displacement are in the direction of pore opening (i.e., the right-handed bundle formed by S6 in the closed conformation is being unwrapped) (Figures 7C and 7D). These ligand-induced conformation changes are consistent with the known functional effects of cAMP to favor voltage-dependent opening (Gauss et al., 1998; Ludwig et al., 1998; Santoro et al., 1998).

Conclusion

Cryo-EM structures have addressed three essential properties of HCN channels. First, we show that these channels, despite

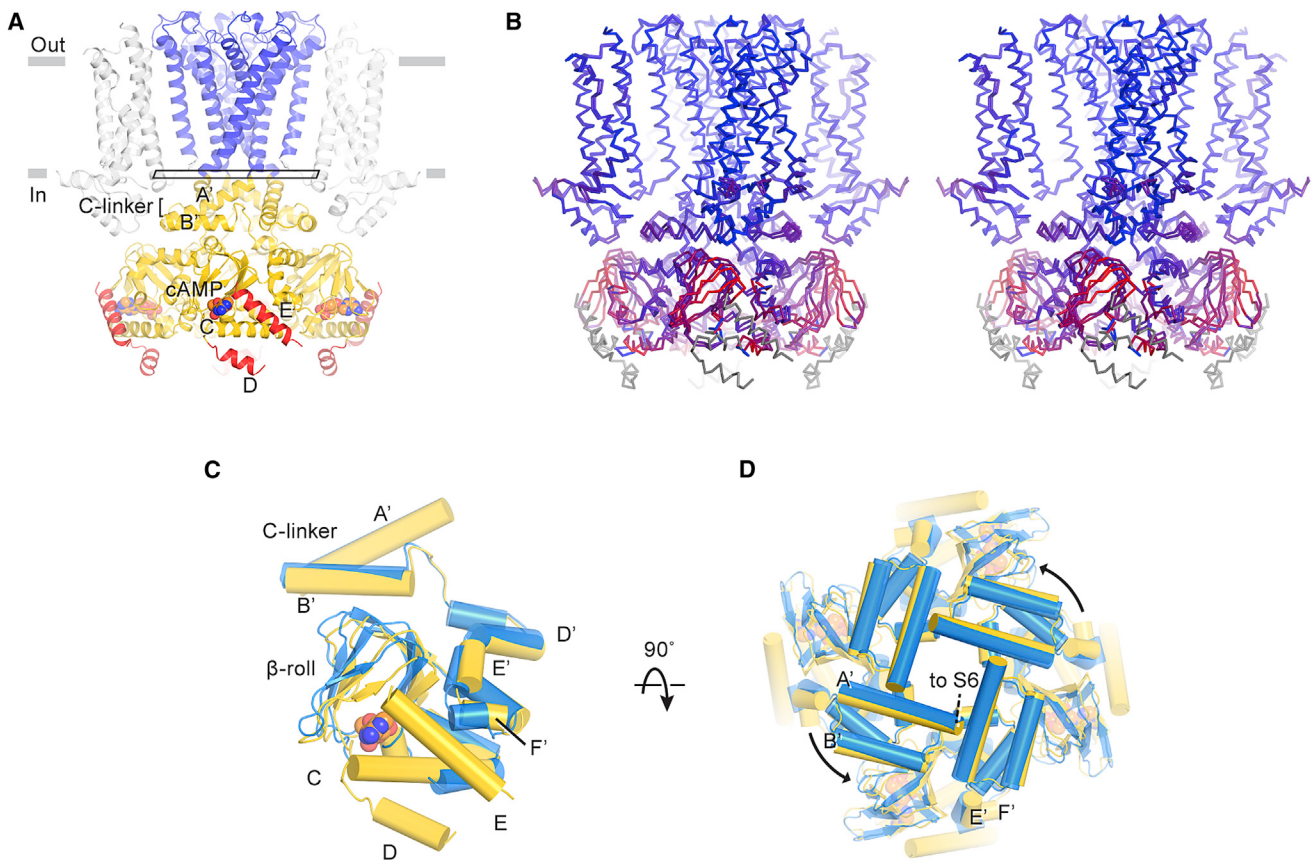


Figure 7. Cyclic AMP Modulation of the HCN1 Channel

(A) Structure of the channel in the cAMP-bound state. D- and E-helices are colored red. The rectangle near the gate indicates the plane of the “slice” used for the view in (D).

(B) Stereo view of the superposition of ligand-free and cAMP-bound structures based on $C\alpha$ atoms of the pore helices. The channel is colored on a red-to-blue spectrum according to the displacement of $C\alpha$ atoms between the two structures. Blue color represents minimal displacements, and red color represents displacements up to 4.5 Å. Gray color indicates residues only present in one structure and thus are not aligned.

(C and D) Superposition of C-linkers and CNBDs in the ligand-free (blue) and cAMP-bound states (yellow). Only single subunits are shown in (C) for clarity. (D) is viewed from the extracellular side.

See also Figures S4 and S7.

having the essential amino acids to form a K^+ selectivity filter, permit Na^+ permeability because the filter adopts a non-canonical conformation that contains two instead of four cation binding sites. The filter structure thus explains Na^+ permeability, which is a fundamental property that enables HCN channels to depolarize a cell's membrane potential.

Second, several unique structural features have led us to posit a plausible hypothesis to explain voltage-dependent gating with reversed polarity. These features include (1) an unusually long S4 helix that contacts a C-linker in the cytoplasm to stabilize a closed gate in the setting of a depolarized voltage sensor, (2) a packing arrangement of S4, S5 and S6 helices that enable the depolarized voltage sensor to stabilize a closed pore, and (3) an HCN domain that also stabilizes the closed pore in the setting of a depolarized voltage sensor. These structural features support a mechanism in which voltage-driven downward displacement of the S4 helix upon membrane hyperpolarization will disrupt these stabilizing interactions, allowing the S6 helices to spontaneously open.

Third, we observe that cAMP binding induces local conformational changes that are propagated to the channel. These initiate a rotation of the gate-forming inner helices toward opening. This would explain why cAMP favors HCN channel opening.

STAR METHODS

Detailed methods are provided in the online version of this paper and include the following:

- KEY RESOURCES TABLE
- CONTACT FOR REAGENT AND RESOURCE SHARING
- EXPERIMENTAL MODEL AND SUBJECT DETAILS
 - Cell lines
- METHOD DETAILS
 - Construct design
 - Electrophysiological recording
 - Protein Expression and purification
 - EM data acquisition

- Image processing
- Model building
- QUANTIFICATION AND STATISTICAL ANALYSIS
- DATA AND SOFTWARE AVAILABILITY
 - Data Resources

SUPPLEMENTAL INFORMATION

Supplemental Information includes seven figures and one table and can be found with this article online at <http://dx.doi.org/10.1016/j.cell.2016.12.023>.

AUTHOR CONTRIBUTIONS

C.-H.L. performed the experiments. C.-H.L. and R.M. designed the experiments, analyzed the results, and prepared the manuscript.

ACKNOWLEDGMENTS

We thank M. Ebrahim at the Evelyn Gruss Lipper Cryo-EM Resource Center at Rockefeller University for assistance in data collection, members of the MacKinnon laboratory and Gary Yellen for helpful discussions, and Jue Chen for comments on the manuscript. This work was supported in part by NIH grant GM43949. C.-H.L. is supported by the Jane Coffin Childs Memorial Fund fellowship (#61-1632). R.M. is an investigator of the Howard Hughes Medical Institute.

Received: November 7, 2016

Revised: November 29, 2016

Accepted: December 15, 2016

Published: January 12, 2017

REFERENCES

- Afonine, P.V., Headd, J.J., Terwilliger, T.C., and Adams, P.D. (2013). New tool: phenix.real_space_refine. *Comput. Crystallogr. Newslett.* 4, 43–44.
- Aggarwal, S.K., and MacKinnon, R. (1996). Contribution of the S4 segment to gating charge in the Shaker K⁺ channel. *Neuron* 16, 1169–1177.
- Barad, B.A., Echols, N., Wang, R.Y.-R., Cheng, Y., DiMaio, F., Adams, P.D., and Fraser, J.S. (2015). EMRinger: side chain-directed model and map validation for 3D cryo-electron microscopy. *Nat. Methods* 12, 943–946.
- Benarroch, E.E. (2013). HCN channels: function and clinical implications. *Neurology* 80, 304–310.
- Biasini, M., Bienert, S., Waterhouse, A., Arnold, K., Studer, G., Schmidt, T., Kiefer, F., Gallo Cassarino, T., Bertoni, M., Bordoli, L., and Schwede, T. (2014). SWISS-MODEL: modelling protein tertiary and quaternary structure using evolutionary information. *Nucleic Acids Res.* 42, W252–W258.
- Brown, H.F., DiFrancesco, D., and Noble, S.J. (1979). How does adrenaline accelerate the heart? *Nature* 280, 235–236.
- Brown, A., Long, F., Nicholls, R.A., Toots, J., Emsley, P., and Murshudov, G. (2015). Tools for macromolecular model building and refinement into electron cryo-microscopy reconstructions. *Acta Crystallogr. D Biol. Crystallogr.* 71, 136–153.
- Cardone, G., Heymann, J.B., and Steven, A.C. (2013). One number does not fit all: mapping local variations in resolution in cryo-EM reconstructions. *J. Struct. Biol.* 184, 226–236.
- Chen, J., Mitcheson, J.S., Tristani-Firouzi, M., Lin, M., and Sanguinetti, M.C. (2001a). The S4-S5 linker couples voltage sensing and activation of pacemaker channels. *Proc. Natl. Acad. Sci. USA* 98, 11277–11282.
- Chen, S., Wang, J., and Siegelbaum, S.A. (2001b). Properties of hyperpolarization-activated pacemaker current defined by coassembly of HCN1 and HCN2 subunits and basal modulation by cyclic nucleotide. *J. Gen. Physiol.* 117, 491–504.
- Chen, V.B., Arendall, W.B., Headd, J.J., Keedy, D.A., Immormino, R.M., Kapral, G.J., Murray, L.W., Richardson, J.S., and Richardson, D.C. (2010). MolPro-
- bility: All-atom structure validation for macromolecular crystallography. *Acta Crystallogr. Sect. D. Biol. Crystallogr.* 66, 12–21.
- Chen, S., McMullan, G., Faruqi, A.R., Murshudov, G.N., Short, J.M., Scheres, S.H.W., and Henderson, R. (2013). High-resolution noise substitution to measure overfitting and validate resolution in 3D structure determination by single particle electron cryomicroscopy. *Ultramicroscopy* 135, 24–35.
- DeBerg, H.A., Bankston, J.R., Rosenbaum, J.C., Brzovic, P.S., Zagotta, W.N., and Stoll, S. (2015). Structural mechanism for the regulation of HCN ion channels by the accessory protein TRIP8b. *Structure* 23, 734–744.
- Decher, N., Chen, J., and Sanguinetti, M.C. (2004). Voltage-dependent gating of hyperpolarization-activated, cyclic nucleotide-gated pacemaker channels: molecular coupling between the S4-S5 and C-linkers. *J. Biol. Chem.* 279, 13859–13865.
- Derebe, M.G., Sauer, D.B., Zeng, W., Alam, A., Shi, N., and Jiang, Y. (2011). Tuning the ion selectivity of tetrameric cation channels by changing the number of ion binding sites. *Proc. Natl. Acad. Sci. USA* 108, 598–602.
- DiFrancesco, J.C., and DiFrancesco, D. (2015). Dysfunctional HCN ion channels in neurological diseases. *Front. Cell. Neurosci.* 6, 174.
- DiFrancesco, D., and Tortora, P. (1991). Direct activation of cardiac pacemaker channels by intracellular cyclic AMP. *Nature* 351, 145–147.
- Doyle, D.A., Morais Cabral, J., Pfuetzner, R.A., Kuo, A., Gulbis, J.M., Cohen, S.L., Chait, B.T., and MacKinnon, R. (1998). The structure of the potassium channel: molecular basis of K⁺ conduction and selectivity. *Science* 280, 69–77.
- Emsley, P., Lohkamp, B., Scott, W.G., and Cowtan, K. (2010). Features and development of Coot. *Acta Crystallogr. Sect. D. Biol. Crystallogr.* 66, 486–501.
- Gauss, R., Seifert, R., and Kaupp, U.B. (1998). Molecular identification of a hyperpolarization-activated channel in sea urchin sperm. *Nature* 393, 583–587.
- Goehring, A., Lee, C.-H., Wang, K.H., Michel, J.C., Claxton, D.P., Baconguis, I., Althoff, T., Fischer, S., Garcia, K.C., and Gouaux, E. (2014). Screening and large-scale expression of membrane proteins in mammalian cells for structural studies. *Nat. Protoc.* 9, 2574–2585.
- Goldschen-Ohm, M.P., Klenchin, V.A., White, D.S., Cowgill, J.B., Cui, Q., Goldsmith, R.H., and Chanda, B. (2016). Structure and dynamics underlying elementary ligand binding events in human pacemaking channels. *eLife* 5, e20797.
- Grant, T., and Grigorieff, N. (2015a). Automatic estimation and correction of anisotropic magnification distortion in electron microscopes. *J. Struct. Biol.* 192, 204–208.
- Grant, T., and Grigorieff, N. (2015b). Measuring the optimal exposure for single particle cryo-EM using a 2.6 Å reconstruction of rotavirus VP6. *eLife* 4, e06980.
- Kaupp, U.B., Niidome, T., Tanabe, T., Terada, S., Bönigk, W., Stühmer, W., Cook, N.J., Kangawa, K., Matsuo, H., Hirose, T., et al. (1989). Primary structure and functional expression from complementary DNA of the rod photoreceptor cyclic GMP-gated channel. *Nature* 342, 762–766.
- Kirchhofer, A., Helma, J., Schmidthals, K., Frauer, C., Cui, S., Karcher, A., Pellici, M., Muyllymans, S., Casas-Deluccchi, C.S., Cardoso, M.C., et al. (2010). Modulation of protein properties in living cells using nanobodies. *Nat. Struct. Mol. Biol.* 17, 133–138.
- Kucukelbir, A., Sigworth, F.J., and Tagare, H.D. (2014). Quantifying the local resolution of cryo-EM density maps. *Nat. Methods* 11, 63–65.
- Kwan, D.C.H., Prole, D.L., and Yellen, G. (2012). Structural changes during HCN channel gating defined by high affinity metal bridges. *J. Gen. Physiol.* 140, 279–291.
- Lockless, S.W. (2015). Determinants of cation transport selectivity: Equilibrium binding and transport kinetics. *J. Gen. Physiol.* 146, 3–13.
- Lolicato, M., Nardini, M., Gazzarrini, S., Möller, S., Bertinetti, D., Herberg, F.W., Bolognesi, M., Martin, H., Fasolini, M., Bertrand, J.A., et al. (2011). Tetramerization dynamics of C-terminal domain underlies isoform-specific cAMP gating in hyperpolarization-activated cyclic nucleotide-gated channels. *J. Biol. Chem.* 286, 44811–44820.

- Long, S.B., Campbell, E.B., and MacKinnon, R. (2005). Voltage sensor of Kv1.2: structural basis of electromechanical coupling. *Science* 309, 903–908.
- Long, S.B., Tao, X., Campbell, E.B., and MacKinnon, R. (2007). Atomic structure of a voltage-dependent K⁺ channel in a lipid membrane-like environment. *Nature* 450, 376–382.
- Ludwig, A., Zong, X., Jeglitsch, M., Hofmann, F., and Biel, M. (1998). A family of hyperpolarization-activated mammalian cation channels. *Nature* 393, 587–591.
- Mastronarde, D.N. (2005). Automated electron microscope tomography using robust prediction of specimen movements. *J. Struct. Biol.* 152, 36–51.
- Mayer, M.L., and Westbrook, G.L. (1983). A voltage-clamp analysis of inward (anomalous) rectification in mouse spinal sensory ganglion neurones. *J. Physiol.* 340, 19–45.
- Murshudov, G.N., Skubák, P., Lebedev, A.A., Pannu, N.S., Steiner, R.A., Nicholls, R.A., Winn, M.D., Long, F., and Vagin, A.A. (2011). REFMAC 5 for the refinement of macromolecular crystal structures. *Acta Crystallogr. Sect. D Biol. Crystallogr.* 67, 355–367.
- Nava, C., Dalle, C., Rastetter, A., Striano, P., de Kovel, C.G.F., Nabuiss, R., Cancès, C., Ville, D., Brilstra, E.H., Gobbi, G., et al.; EuroEPINOMICS RES Consortium (2014). De novo mutations in HCN1 cause early infantile epileptic encephalopathy. *Nat. Genet.* 46, 640–645.
- Neyton, J., and Miller, C. (1988). Potassium blocks barium permeation through a calcium-activated potassium channel. *J. Gen. Physiol.* 92, 549–567.
- Nicholls, R.A., Fischer, M., McNicholas, S., and Murshudov, G.N. (2014). Conformation-independent structural comparison of macromolecules with ProSMART. *Acta Crystallogr. Sect. D Biol. Crystallogr.* 70, 2487–2499.
- Nishida, M., Cadene, M., Chait, B.T., and MacKinnon, R. (2007). Crystal structure of a Kir3.1-prokaryotic Kir channel chimera. *EMBO J.* 26, 4005–4015.
- Pettersen, E.F., Goddard, T.D., Huang, C.C., Couch, G.S., Greenblatt, D.M., Meng, E.C., and Ferrin, T.E. (2004). UCSF Chimera—a visualization system for exploratory research and analysis. *J. Comput. Chem.* 25, 1605–1612.
- Postea, O., and Biel, M. (2011). Exploring HCN channels as novel drug targets. *Nat. Rev. Drug Discov.* 10, 903–914.
- Puljung, M.C., DeBerg, H.A., Zagotta, W.N., and Stoll, S. (2014). Double electron-electron resonance reveals cAMP-induced conformational change in HCN channels. *Proc. Natl. Acad. Sci. USA* 111, 9816–9821.
- Rothberg, B.S., Shin, K.S., and Yellen, G. (2003). Movements near the gate of a hyperpolarization-activated cation channel. *J. Gen. Physiol.* 122, 501–510.
- Santoro, B., Liu, D.T., Yao, H., Bartsch, D., Kandel, E.R., Siegelbaum, S.A., and Tibbs, G.R. (1998). Identification of a gene encoding a hyperpolarization-activated pacemaker channel of brain. *Cell* 93, 717–729.
- Santoro, B., Piskorowski, R.A., Pian, P., Hu, L., Liu, H., and Siegelbaum, S.A. (2009). TRIP8b splice variants form a family of auxiliary subunits that regulate gating and trafficking of HCN channels in the brain. *Neuron* 62, 802–813.
- Saponaro, A., Pauleta, S.R., Cantini, F., Matzapetakis, M., Hammann, C., Donadoni, C., Hu, L., Thiel, G., Banci, L., Santoro, B., and Moroni, A. (2014). Structural basis for the mutual antagonism of cAMP and TRIP8b in regulating HCN channel function. *Proc. Natl. Acad. Sci. USA* 111, 14577–14582.
- Scheres, S.H.W. (2012). RELION: implementation of a Bayesian approach to cryo-EM structure determination. *J. Struct. Biol.* 180, 519–530.
- Scheres, S.H.W. (2014). Beam-induced motion correction for sub-megadalton cryo-EM particles. *eLife* 3, e03665.
- Scheres, S.H.W., and Chen, S. (2012). Prevention of overfitting in cryo-EM structure determination. *Nat. Methods* 9, 853–854.
- Seoh, S.A., Sigg, D., Papazian, D.M., and Bezanilla, F. (1996). Voltage-sensing residues in the S2 and S4 segments of the Shaker K⁺ channel. *Neuron* 16, 1159–1167.
- Shealy, R.T., Murphy, A.D., Ramarathnam, R., Jakobsson, E., and Subramanian, S. (2003). Sequence-function analysis of the K⁺-selective family of ion channels using a comprehensive alignment and the KcsA channel structure. *Biophys. J.* 84, 2929–2942.
- Shi, N., Ye, S., Alam, A., Chen, L., and Jiang, Y. (2006). Atomic structure of a Na⁺- and K⁺-conducting channel. *Nature* 440, 570–574.
- Smart, O.S., Neduvelli, J.G., Wang, X., Wallace, B.A.A., and Sansom, M.S.P. (1996). HOLE: a program for the analysis of the pore dimensions of ion channel structural models. *J. Mol. Graph.* 14, 354–360, 376.
- Tang, G., Peng, L., Baldwin, P.R., Mann, D.S., Jiang, W., Rees, I., and Ludtke, S.J. (2007). EMAN2: an extensible image processing suite for electron microscopy. *J. Struct. Biol.* 157, 38–46.
- Tao, X., Lee, A., Limapichat, W., Dougherty, D.A., and MacKinnon, R. (2010). A gating charge transfer center in voltage sensors. *Science* 328, 67–73.
- Tibbs, G.R., Posson, D.J., and Goldstein, P.A. (2016). Voltage-Gated Ion Channels in the PNS: Novel Therapies for Neuropathic Pain? *Trends Pharmacol. Sci.* 37, 522–542.
- Verkerk, A.O., and Wilders, R. (2015). Pacemaker activity of the human sinoatrial node: an update on the effects of mutations in HCN4 on the hyperpolarization-activated current. *Int. J. Mol. Sci.* 16, 3071–3094.
- Wainger, B.J., DeGennaro, M., Santoro, B., Siegelbaum, S.A., and Tibbs, G.R. (2001). Molecular mechanism of cAMP modulation of HCN pacemaker channels. *Nature* 411, 805–810.
- Whicher, J.R., and MacKinnon, R. (2016). Structure of the voltage-gated K⁺ channel Eag1 reveals an alternative voltage sensing mechanism. *Science* 353, 664–669.
- Yellen, G. (1984). Relief of Na⁺ block of Ca²⁺-activated K⁺ channels by external cations. *J. Gen. Physiol.* 84, 187–199.
- Zagotta, W.N., Olivier, N.B., Black, K.D., Young, E.C., Olson, R., and Gouaux, E. (2003). Structural basis for modulation and agonist specificity of HCN pacemaker channels. *Nature* 425, 200–205.
- Zhang, K. (2016). Gctf: Real-time CTF determination and correction. *J. Struct. Biol.* 193, 1–12.
- Zhou, M., and MacKinnon, R. (2004). A mutant KcsA K(+) channel with altered conduction properties and selectivity filter ion distribution. *J. Mol. Biol.* 338, 839–846.
- Zhou, Y., Morais-Cabral, J.H., Kaufman, A., and MacKinnon, R. (2001). Chemistry of ion coordination and hydration revealed by a K⁺ channel-Fab complex at 2.0 Å resolution. *Nature* 414, 43–48.
- Zolles, G., Wenzel, D., Bildl, W., Schulte, U., Hofmann, A., Müller, C.S., Thumfarth, J.-O., Vlachos, A., Deller, T., Pfeifer, A., et al. (2009). Association with the auxiliary subunit PEX5R/Trip8b controls responsiveness of HCN channels to cAMP and adrenergic stimulation. *Neuron* 62, 814–825.

STAR★METHODS

KEY RESOURCES TABLE

REAGENT or RESOURCE	SOURCE	IDENTIFIER
Chemicals, Peptides, and Recombinant Proteins		
DMEM/F-12 medium	GIBCO	11330-032
Sf-900 II SFM medium	GIBCO	10902-088
Freestyle 293 medium	GIBCO	12338-018
Lipofectamine 3000 reagent	Invitrogen	L3000015
Cellfectin II reagent	Invitrogen	10362100
lauryl maltose neopentyl glycol	Anatrace	NG310
Cholesteryl hemisuccinate	Anatrace	CH210
Digitonin	Calbiochem	300410
3', 5'-cyclic AMP sodium salt	Sigma-Aldrich	A6885
Critical Commercial Assays		
CNBR-activated Sepharose beads	GE Healthcare	17-0430-01
Superose 6, 10/300 GL	GE Healthcare	17-5172-01
Deposited Data		
Human HCN1 _{EM} density map	This study	EMDB: EMD-8511
Human HCN1 _{EM} with cAMP density map	This study	EMDB: EMD-8512
Human HCN1 _{EM} atomic model	This study	PDB: 5U6O
Human HCN1 _{EM} with cAMP atomic model	This study	PDB: 5U6P
Experimental Models: Cell Lines		
CHO-K1	ATCC	CRL-9618
Sf9	ATCC	CRL-1711
HEK293S GnT ⁻	ATCC	CRL-3022
Recombinant DNA		
Human HCN1 _{EM}	This study	N/A
Software and Algorithms		
Serial EM	Mastronarde, 2005	http://bio3d.colorado.edu/SerialEM
Unblur	Grant and Grigorieff, 2015b	http://grigoriefflab.janelia.org/unblur
Gctf	Zhang, 2016	http://www.mrc-lmb.cam.ac.uk/kzhang/
RELION	Scheres, 2012	http://www2.mrc-lmb.cam.ac.uk/relion
Gautomatch	Kai Zhang	http://www.mrc-lmb.cam.ac.uk/kzhang/
EMAN2	Tang et al., 2007	http://blakebcm.edu/emanwiki/EMAN2
Blocres	Cardone et al., 2013	https://lsbr.niams.nih.gov/bsoft/programs/blocres.html
ResMap	Kucukelbir et al., 2014	http://resmap.sourceforge.net/
SWISS-MODEL	Biasini et al., 2014	https://swissmodel.expasy.org/
UCSF Chimera	Pettersen et al., 2004	http://www.cgl.ucsf.edu/chimera
PHENIX	Afonine et al., 2013	https://www.phenix-online.org
COOT	Emsley et al., 2010	http://www2.mrc-lmb.cam.ac.uk/personal/pemsley/coot/
REFMAC	Brown et al., 2015; Murshudov et al., 2011	https://www2.mrc-lmb.cam.ac.uk/groups/murshudov/content/em_fitting/em_fitting.html
ProSMART	Nicholls et al., 2014	https://www2.mrc-lmb.cam.ac.uk/groups/murshudov/content/prosmart/prosmart.html

(Continued on next page)

Continued

REAGENT or RESOURCE	SOURCE	IDENTIFIER
MolProbity	Chen et al., 2010	http://molprobity.biochem.duke.edu
EMRinger	Barad et al., 2015	http://fraserlab.com/2015/02/18/EMringer/
HOLE	Smart et al., 1996	http://www.holeprogram.org/
PyMOL	Molecular Graphics System, Version 1.8 Schrodinger, LLC	http://www.pymol.org
Other		
R1.2/1.3 400 mesh Au holey carbon grids	Quantifoil	1210627

CONTACT FOR REAGENT AND RESOURCE SHARING

Requests for reagents may be directed to the lead contact Roderick MacKinnon (mackinn@rockefeller.edu)

EXPERIMENTAL MODEL AND SUBJECT DETAILS**Cell lines**

Chinese hamster ovary (CHO)-K1 cells were cultured in DMEM/F-12 medium (GIBCO) supplemented with 10% fetal bovine serum at 37°C. Sf9 cells were cultured in Sf-900 II SFM medium (GIBCO) at 28°C. HEK293S GnT⁻ cells were cultured in Freestyle 293 medium supplemented with 2% fetal bovine serum at 37°C.

METHOD DETAILS**Construct design**

A DNA segment encoding the human HCN1 channel was synthesized and cloned into a pEG BacMam vector (Goehring et al., 2014), where HCN1 is placed after an N-terminal green fluorescent protein (GFP) tag and a PreScission protease cleavage site. To improve the biochemical stability and expression level of HCN1, we truncated a segment near its C terminus (amino acid residues 636–865), which is only present in HCN1 but not HCN2–4. This construct, denoted HCN1_{EM} (Figure S1), was used in all following experiments.

Electrophysiological recording

CHO-K1 cells were cultured on coverslips placed in a 6-well plate. Cells in each well were transiently transfected with 2 µg plasmid DNA of HCN1_{EM} using Lipofectamine 3000 (Invitrogen) according to the manufacturer's instructions. After 36–60 hr, the coverslips were transferred to a recording chamber containing the external solution (55 mM KCl, 100 mM NaCl, 1 mM CaCl₂, 10 mM glucose, and 10 mM HEPES pH 7.4; 310 mOsm). Borosilicate micropipettes (OD 1.5mm, ID 0.86 mm, Sutter) were pulled and fire polished. Pipettes were then filled with the internal solution (85 mM KCl, 70 mM KF, 5 mM EGTA, and 10 mM HEPES pH 7.2; 297 mOsm). Where indicated, the internal solution also contained 500 µM cAMP (as a sodium salt). Pipettes had a resistance of 2–5 MΩ. Whole-cell recordings were obtained at room temperature (~23°C) using an Axopatch 200B amplifier, a Digidata 1550 digitizer and pCLAMP software (Molecular Devices). The recordings were low-pass filtered at 1 kHz and sampled at 20 kHz. The cells were initially held at –30 mV. To obtain the activation curves, cells were hyperpolarized from –30 to –130 mV in 10 mV decrements, followed by a test pulse at –130 mV (Figures S2A and S2B). To measure the reversal potential, cells were first hyperpolarized to –130 mV, followed by a series of test pulses from 30 to –130 mV in 20 mV decrements (Figures S2C and S2D). The permeability ratio of K⁺ over Na⁺ (P_K/P_{Na}) was calculated using the Goldman-Hodgkin-Katz equation. Nonlinear regressions were performed in Prism (GraphPad).

Protein Expression and purification

HCN1_{EM} was expressed in HEK293S GnT⁻ cells using BacMam method (Goehring et al., 2014). Briefly, a bacmid carrying HCN1_{EM} was generated by transforming *E. coli* DH10Bac cells with the HCN1_{EM} construct according to the manufacturer's instructions (Bac-to-Bac; Invitrogen). Baculoviruses were produced by transfecting *Spodoptera frugiperda* Sf9 cells with the bacmid using Cellfectin II (Invitrogen). Baculoviruses after two rounds of amplification were used for cell transduction. Suspension cultures of HEK293S GnT⁻ cells were grown at 37°C to a density of ~3 × 10⁶ cells/ml and baculoviruses were added (10%–12% v/v) to initiate the transduction. After 12 hr, 10 mM sodium butyrate was supplemented and the temperature was shifted to 30°C. Cells were harvested at 60 hr post-transduction.

HCN1_{EM} protein was purified at 4°C. The cell pellet from 1 L culture was resuspended in 5mL of 30% glycerol for 10 min. The cell suspension was then mixed with 200mL hypotonic lysis buffer (20 mM KCl, 0.5 mM MgCl₂, 2 mM DTT, 0.1 mg/ml DNase, and 10 mM Tris pH 8) for 25 min, and the lysate was spun at 39800 x g for 35 min to sediment crude membranes. The membrane pellet was mechanically homogenized and solubilized in extraction buffer (10 mM lauryl maltose neopentyl glycol, 2 mM cholesteryl hemisuccinate, 300 mM KCl, 2 mM DTT, and 20 mM Tris pH 8) for 1.5 hr. Solubilized membranes were clarified by centrifugation at 39800 x g for

35 min. The supernatant was applied to the GFP nanobody-coupled Sepharose resin (Kirchhofer et al., 2010), which was subsequently washed with 10 column volumes of wash buffer (0.05% digitonin, 300 mM KCl, 2 mM DTT, and 20 mM Tris pH 8). The washed resin was incubated overnight with PreScission protease at a target protein to protease ratio of 40:1 (w/w) to cleave off GFP and release the protein from the resin. The protein was eluted with wash buffer, concentrated by Amicon Ultra centrifugal filter (MWCO 100 kDa), and then injected to a Superose 6 column (GE Healthcare) equilibrated with SEC buffer (0.05% digitonin, 150 mM KCl, 2 mM DTT, and 20 mM Tris pH 8) (Figures S2E and S2F). Peak fractions were pooled and concentrated to 4–5 mg/ml. All buffers contain protease inhibitors (2 µg/ml leupeptin, 1 µg/ml pepstatin, 50 µg/ml benzamidine, 10 µg/ml aprotinin, and 1 mM AEBSF). To purify the channel in the cAMP-bound state, 0.1% digitonin and 300 mM KCl were used in the wash and SEC buffer, and all buffers were supplemented with 5 µM cAMP. In addition, 5 mM cAMP was spiked to the protein sample prior to EM grid preparation.

EM data acquisition

3.5 µL of purified HCN channel samples at 4–5 mg/ml were applied to glow-discharged Quantifoil R1.2/1.3 400 mesh Au grids. After a 15 s incubation, the grids were blotted for 1 s and plunged into liquid ethane, using a Vitrobot Mark IV (FEI) operated at 22°C and 100% humidity. The grids were then loaded onto a Titan Krios transmission electron microscope (FEI) operated at 300 keV. Micrographs were recorded on a K2 Summit direct electron detector (Gatan) in super-resolution counting mode using SerialEM (Mastronarde, 2005). Images have a calibrated physical pixel size of 1.3 Å (a super-resolution pixel size of 0.65 Å) and a nominal defocus range of −1.5 to −3.3 µm. For the ligand-free dataset, a dose rate of 8.5 electrons per pixel per second was used. The exposure time for each image was 10 s fractionated over 40 frames, resulting in a total cumulative dose of ~50 electrons per Å² (1.26 electrons per Å² per frame). For the cAMP dataset, a dose rate of 10 electrons per pixel per second was used. The exposure time for each image was 15 s fractionated over 50 frames, resulting in a total cumulative dose of ~89 electrons per Å² (1.78 electrons per Å² per frame). Acquisition parameters are summarized in Table S1.

Image processing

Super-resolution image frames were gain-normalized and binned 2 by 2 to a pixel size of 1.3 Å with Fourier cropping (Grant and Grigorieff, 2015a). The frames were then aligned using UnBlur (Grant and Grigorieff, 2015b) to correct beam-induced motions. Gctf (Zhang, 2016) was used to estimate the defocus parameters on the summed image of motion-corrected frames generated by UnBlur. The summed image of motion-corrected frames after the exposure filter (also by UnBlur) was subjected to subsequent processing in RELION (Scheres, 2012). About 3,000 particles were manually picked and processed by reference-free 2D classification in RELION to generate 7 classes for templated-based particle picking using Gautomatch (written by Kai Zhang). Auto-picked particles were visually examined to remove false positives and further cleaned up by multiple rounds of 2D classification. An initial 3D model with C4 symmetry was generated from representative 2D class averages by EMAN2 (Tang et al., 2007). For the ligand-free dataset, a 3D classification into four classes was carried out without applying symmetry in RELION. The major class (53% of the input; 55,870 particles) contained the most structural details and was refined to 3.6 Å resolution. These particles were subjected to particle-based motion correction and radiation-damage weighing (particle polishing) in RELION (Scheres, 2014). The ‘shiny’ particles were used for the final reconstruction, resulting in a map of overall 3.5 Å resolution. For the cAMP dataset, particles from two sessions of data collection were first processed separately. Particles of session 1 were subjected to two rounds of 3D classification into ten classes without applying symmetry. The classes with the most structural details were combined (36% of the input; 103,356 particles) and refined to 4.2 Å. The particle polishing improved the resolution to 3.9 Å. The 103,356 particles were subjected to another 3D classification into nine classes without alignment. Two major resulting classes were combined (94,222 particles) and refined to 3.8 Å resolution. Particles of session 2 were subjected to a 3D classification into six classes without applying symmetry. Three major classes were combined (61% of the input; 110,341 particles) and refined to 3.9 Å resolution. The particle polishing improved the resolution to 3.6 Å. At this stage, particles from session 1 and 2 were merged and subjected to another 3D classification into eight classes without alignment. Two major resulting classes were combined (125,339 particles) and refined to 3.5 Å resolution. All refinements were performed with C4 symmetry imposed and followed the gold-standard Fourier shell correlation (FSC) procedure (Scheres and Chen, 2012). The FSC curves were calculated with soft masks that exclude the detergent micelles and the effects of masking were corrected by the post-processing procedure in RELION (Chen et al., 2013). The reported resolutions were based on the FSC = 0.143 criterion on corrected FSC curves (Figures S3D, S4D, and Table S1). Local resolutions of unfiltered density maps were estimated by Blocres (Cardone et al., 2013) with a kernel size of 16 or by ResMap (Kucukelbir et al., 2014). In both datasets, ResMap estimated higher resolutions and most regions fell between 3.0–3.5 Å. Only the estimations from Blocres were shown (Figures S3F and S4F).

Model building

A homology model for one subunit of the transmembrane domains was generated by SWISS-MODEL server (Biasini et al., 2014) using the Eag1 channel as a reference (Whicher and MacKinnon, 2016). This homology model and the crystal structure of mouse HCN1 cytoplasmic domains (Lolicato et al., 2011) (PDB ID: 3U0Z) were docked into the summed density map of the cAMP dataset using UCSF chimera (Pettersen et al., 2004). A tetramer model of the channel was obtained by a symmetry operation of the monomer. The model was first refined with phenix.real_space_refine (Afonine et al., 2013). Subsequent model building and real space refinement were done in COOT (Emsley et al., 2010). The resulting model was used as an initial model for the ligand-free structure, which

was then refined and rebuilt following the same procedure. Both tetramer models were further refined against their respective summed maps in reciprocal space using REFMAC v5.8 with a script developed for cryo-EM model refinements (Brown et al., 2015; Murshudov et al., 2011) (Table S1). 4-fold symmetry was imposed during refinement using strong non-crystallographic symmetry restraints. Secondary structure restraints generated by ProSMART were also applied (Nicholls et al., 2014). A refinement weight of 0.001 or 0.0005 was used for the ligand-free dataset or cAMP dataset, respectively. For cross-validation (Brown et al., 2015), the refined structures were randomly displaced up to 0.5 Å. The displaced models were then refined against one of the two half maps produced by RELION. The FSC_{half1} curves were calculated between the refined models and the half maps used during refinement. The FSC_{half2} curves were calculated between the refined models and the other half maps not used during the refinement. Small differences between FSC_{half1} and FSC_{half2} suggest that the models were not over fitted (Figures S3E and S4E). The final ligand-free structure includes residues 94–200, 203–242, and 252–586, whereas the cAMP-bound structure includes additional residues 587–608 and the E-helices (Figure S1). Side chains were not modeled for residues with poor density. In the cAMP-bound structure, we could not accurately register the E-helix, which was thus built as a separate, polyalanine chain for each subunit (chain E, F, G, and H). The quality of the final models was evaluated by MolProbity (Chen et al., 2010) and EMRinger (Barad et al., 2015) (Table S1). The pore radius was calculated by HOLE (Smart et al., 1996). Figures were prepared using the PyMOL Molecular Graphics System, Version 1.8 Schrodinger, LLC.

QUANTIFICATION AND STATISTICAL ANALYSIS

See [Methods Details](#) for details on cryo-EM analysis.

DATA AND SOFTWARE AVAILABILITY

Data Resources

Cryo-EM density maps of HCN1 and HCN1 in the cAMP-bound state have been deposited in the electron microscopy data bank under accession code EMD-8511 and EMD-8512, respectively. Atomic coordinates of HCN1 and HCN1 in the cAMP-bound state have been deposited in the protein data bank under accession code 5U6O and 5U6P, respectively.

Supplemental Figures

Cell

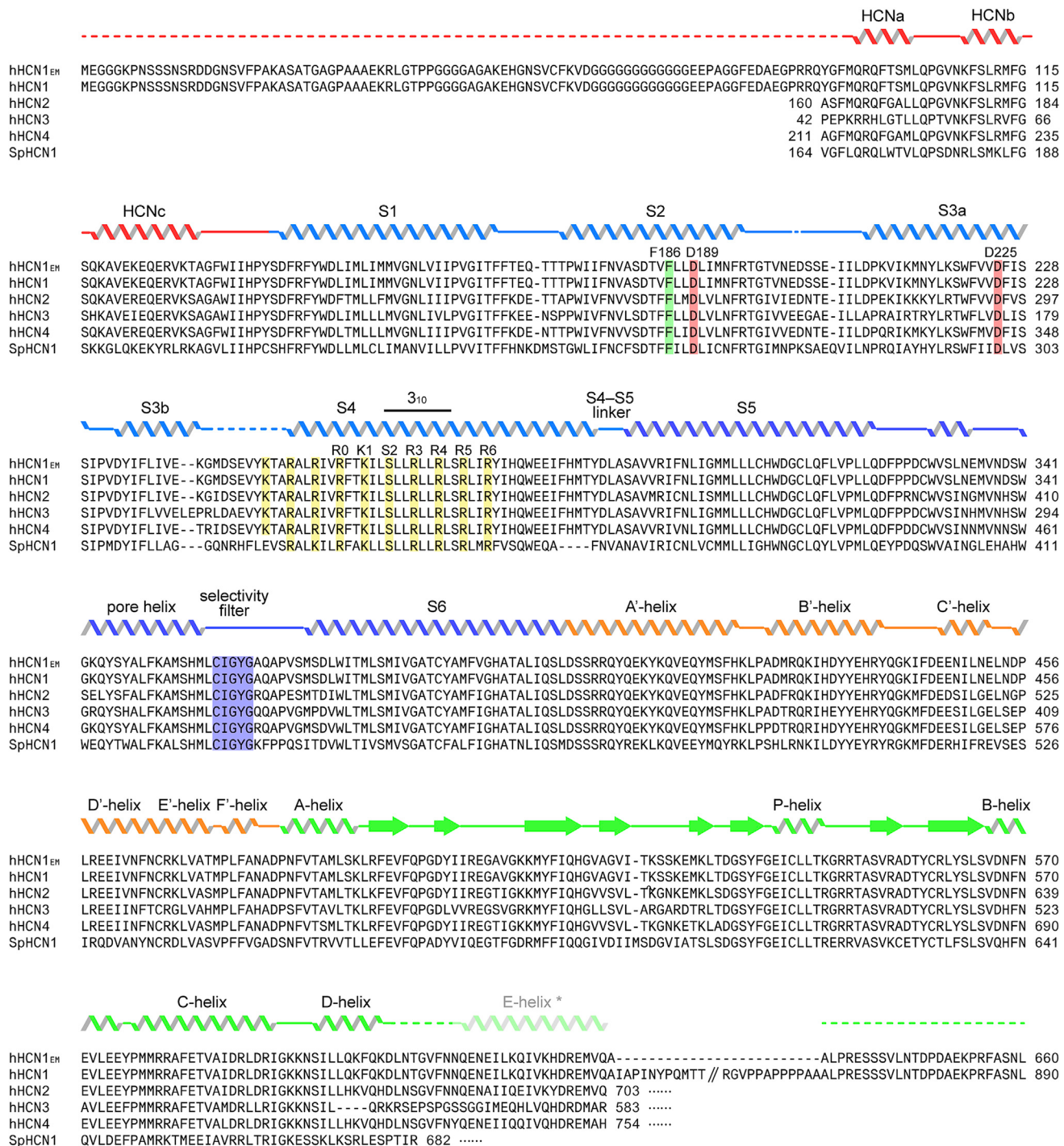


Figure S1. Sequence Alignment of HCN Channels, Related to Figure 1

The full-length human HCN1 and core regions of human HCN2–4 (hHCN1–4) and sea urchin HCN1 (SpHCN1) are shown. Secondary structures are represented by ribbons (α helices), arrows (β strands), and loops (loops). Residues of the human HCN1_{EM} (hHCN1_{EM}) construct not modeled in the cryo-EM structures are denoted by dash lines. Relevant residues are labeled and numbered based on the human HCN1 (hHCN1) sequence. For brevity, a portion of the hHCN1 sequence at the C terminus is removed (represented by //). A precise registration of the E-helix is not feasible for the current study, which is indicated by an asterisk (*). Amino acid sequences are from UniProtKB using the following entries: hHCN1, O60741; hHCN2, Q9UL51; hHCN3, Q9P1Z3; hHCN4, Q9Y3Q4; and SpHCN1, O76977.

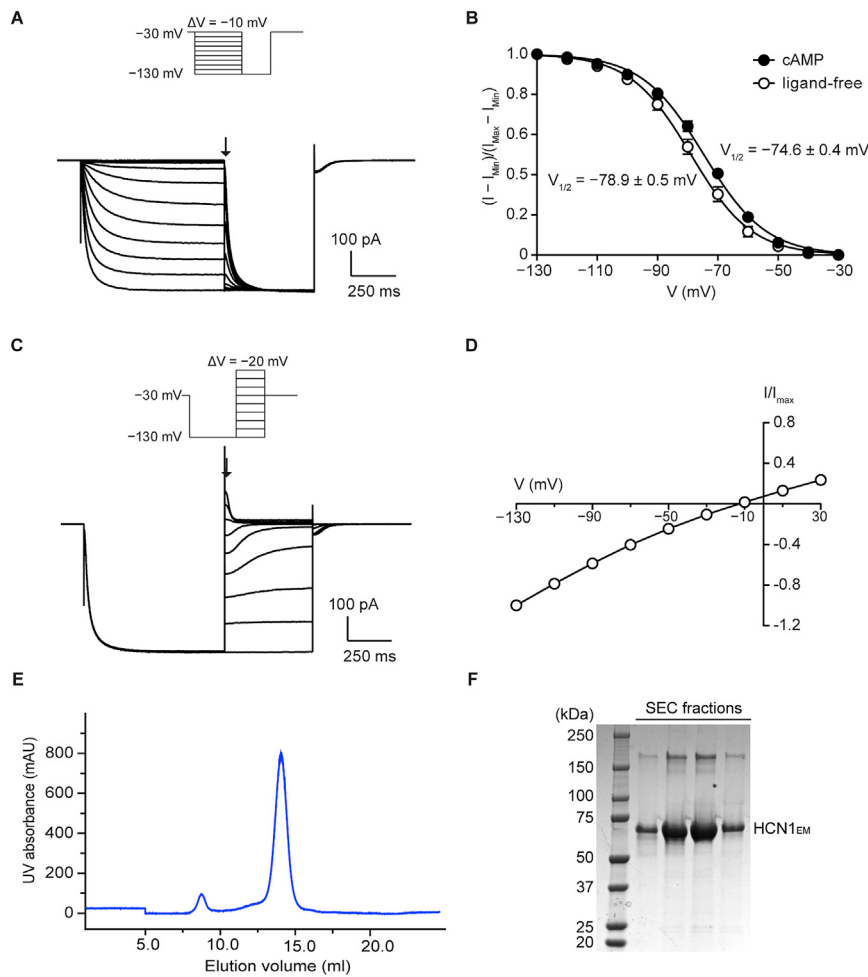


Figure S2. Functional and Biochemical Characterization of Human HCN1_{EM}, Related to Figure 1

(A) Voltage-dependent activation of HCN1_{EM}. A representative electrophysiological recording from the CHO-K1 cell expressing HCN1_{EM} is shown. Tail currents used to generate activation curves are indicated by an arrow.

(B) Activation curves of HCN1_{EM} in the absence or presence of internal cAMP. Fraction of the maximum current ($n = 6-11$; means \pm SEM) is plotted against the hyperpolarization voltage and fitted with a single Boltzmann function to obtain the midpoint voltage ($V_{1/2}$).

(C and D) Ion selectivity of HCN1_{EM}. A representative recording is shown in (C). Tail currents used to estimate the reversal potential are indicated by an arrow. In (D), fraction of the normalized current ($n = 6$; means \pm SEM) is plotted against the holding voltage to show the reversal potential of HCN1_{EM}. The current for each holding voltage is normalized to the current at -130 mV . The calculated P_K/P_{Na} is about 3.

(E) Representative size-exclusion chromatography (SEC) trace of HCN1_{EM}. Peak fractions were used for cryo-EM analysis.

(F) SDS-PAGE gel of peak fractions stained with Coomassie blue. The predicted molecular weight based on protein sequence for a single HCN1_{EM} subunit is 75 kDa.

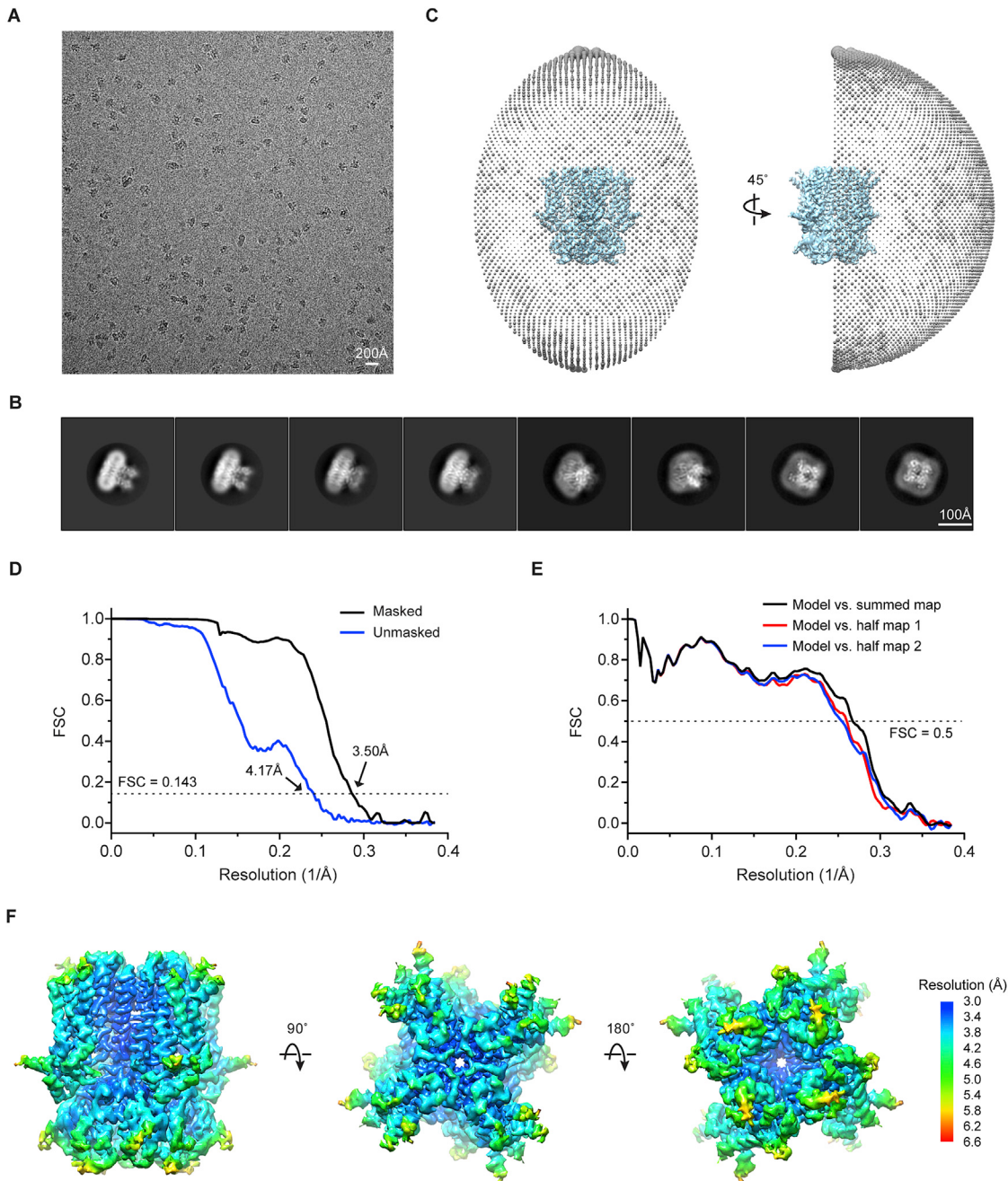


Figure S3. Single-Particle Cryo-EM of the HCN Channel in the Ligand-Free State, Related to Figure 1

(A) Representative raw micrograph of the channel in the ligand-free state.

(B) Selected 2D class averages.

(C) Euler angle distribution of particles for the final 3D reconstruction. The radius of the gray sphere is proportional to the number of particles assigned to that specific orientation.

(D) Fourier shell correlation (FSC) curves between two half maps before (blue) and after (black) the post-processing in RELION.

(E) FSC curves for cross-validation: model versus summed map (black), model versus half map 1 (FSC_{half1} , red), model versus half map 2 (FSC_{half2} , blue). The model was refined against half map 1 but not half map 2. Small differences between the FSC_{half1} and FSC_{half2} curves suggest little effect of over-fitting.

(F) Local resolution of density map estimated by Blocres. The map shown is low-pass filtered to 3.50 Å and sharpened with a b-factor of -90 \AA^2 .

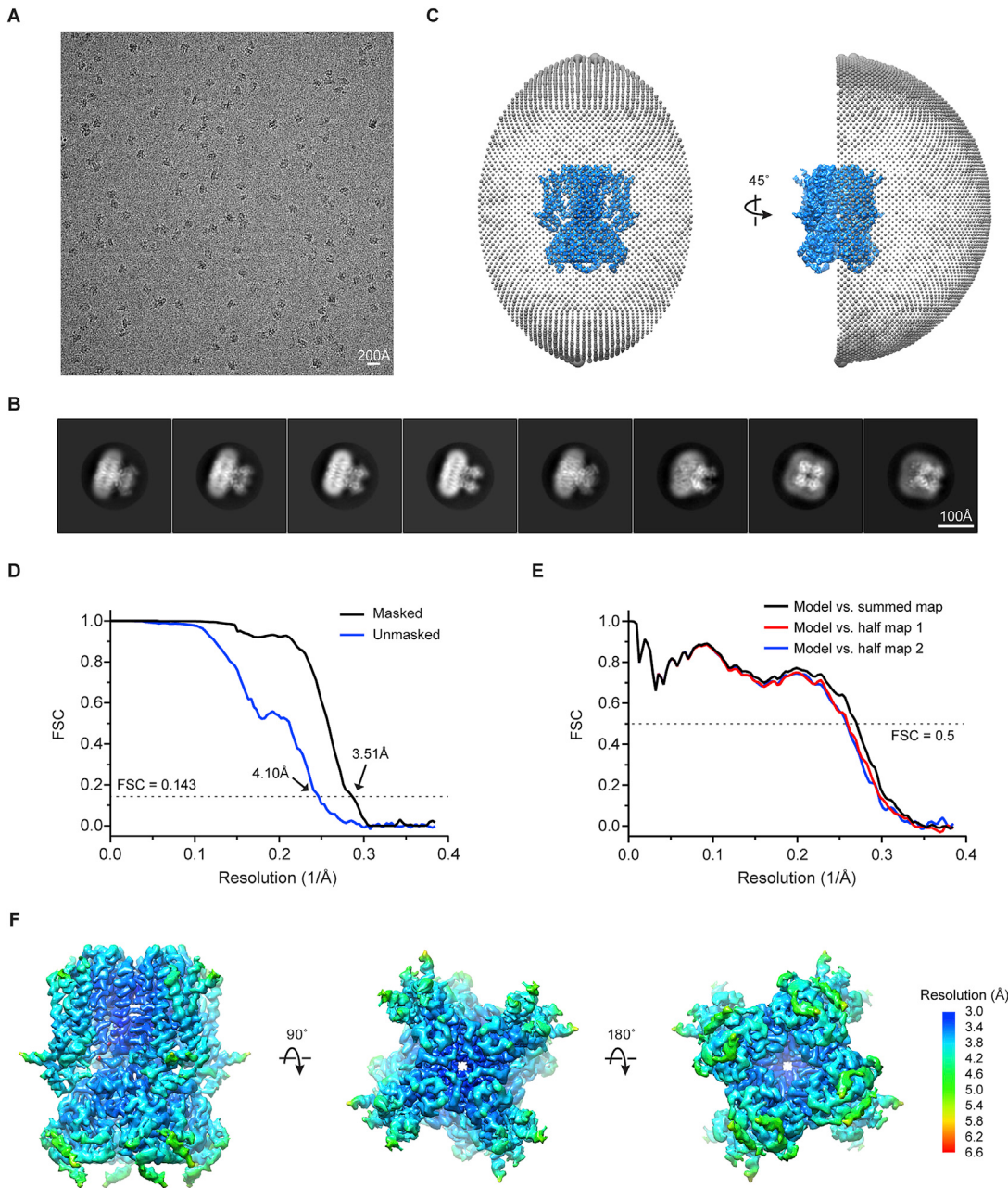


Figure S4. Single-Particle Cryo-EM of the HCN1 Channel in the cAMP-Bound State, Related to Figures 6 and 7

(A) Representative raw micrograph of the channel in the cAMP-bound state.

(B) Selected 2D class averages.

(C) Euler angle distribution of particles for the final 3D reconstruction. The radius of the gray sphere is proportional to the number of particles assigned to that specific orientation.

(D) Fourier shell correlation (FSC) curves between two half maps before (blue) and after (black) the post-processing in RELION.

(E) FSC curves for cross-validation: model versus summed map (black), model versus half map 1 (FSC_{half1} , red), model versus half map 2 (FSC_{half2} , blue). The model was refined against half map 1 but not half map 2. Small differences between the FSC_{half1} and FSC_{half2} curves suggest little effect of over-fitting.

(F) Local resolution of density map estimated by Blocres. The map shown is low-pass filtered to 3.51 Å and sharpened with a b-factor of -120 \AA^2 .

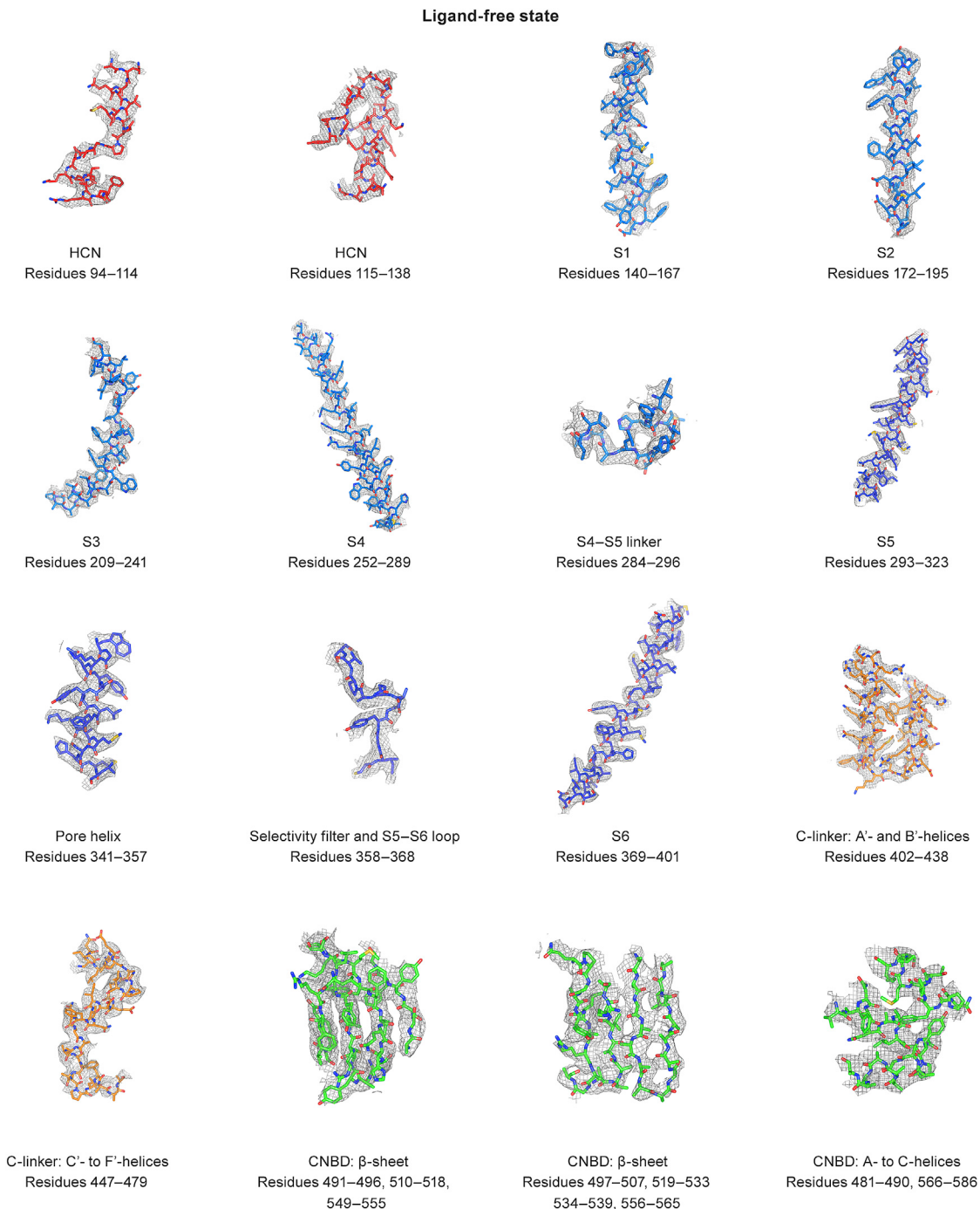


Figure S5. EM Density of the HCN1 Channel in the Ligand-Free State, Related to Figure 1

The atomic model of each domain is in different colors (HCN domain, red; S1–S4, blue; S5–S6, purple; C-linker, orange; and CNBD, green). For the S4–S5 linker, residues from S4 and S5 helices are also included to emphasize the continuity of the density at this region. The map is low-pass filtered to 3.50 Å, sharpened with a b-factor of -90 \AA^2 , and contoured at 5.5–6 σ .

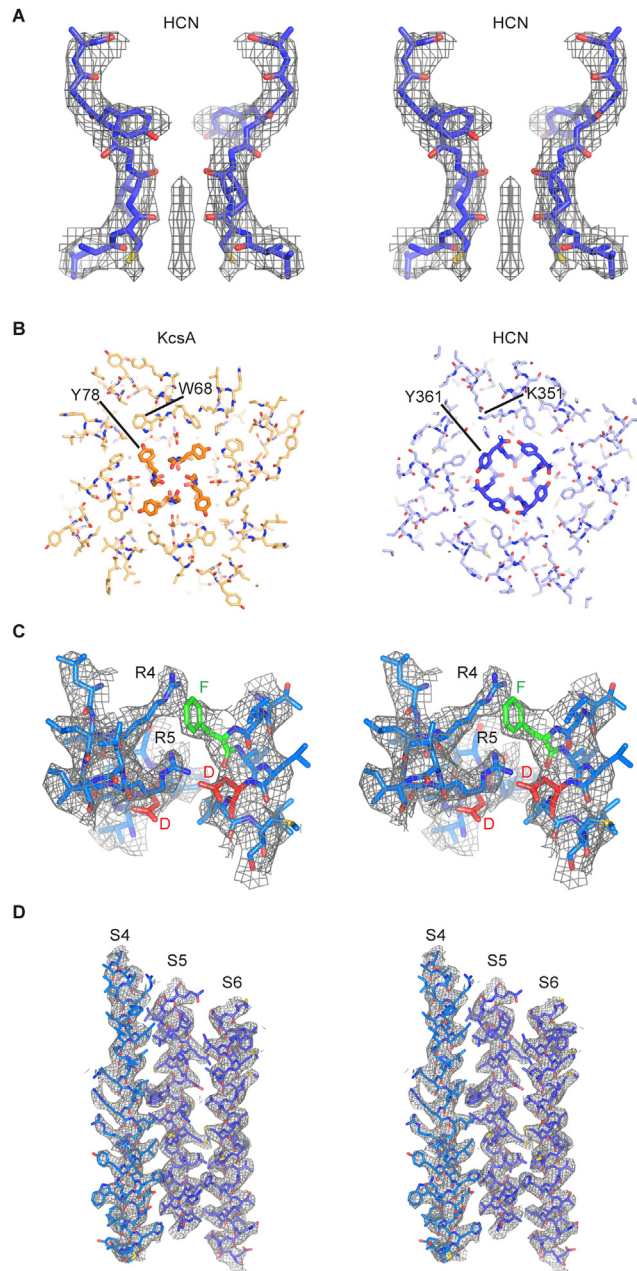


Figure S6. Structural Details of HCN1 Selectivity Filter, Gating Charge Transfer Center, and the Packing of S4–S6 Helices, Related to Figures 2, 4, and 5

(A) Stereo view of the selectivity filter in the HCN1 channel. Only two subunits of the channel are shown. The density map (gray mesh) is sharpened with a b-factor of -120 \AA^2 and contoured at 5.5σ .

(B) Cross section of KcsA and HCN1 channels viewed from the extracellular side, showing the packing of residues (thin sticks) surrounding the selectivity filter (thick sticks). Residues W68 and Y78 in the KcsA channel correspond to residues K351 and Y361 in the HCN1 channel.

(C) Stereo view of the gating charge transfer center in the HCN1 channel. The density map (gray mesh) is sharpened with a b-factor of -90 \AA^2 and contoured at 5.5σ .

(D) Stereo view of S4–S6 helices in the HCN1 channel. The density map (gray mesh) is sharpened with a b-factor of -90 \AA^2 and contoured at 5.5σ .

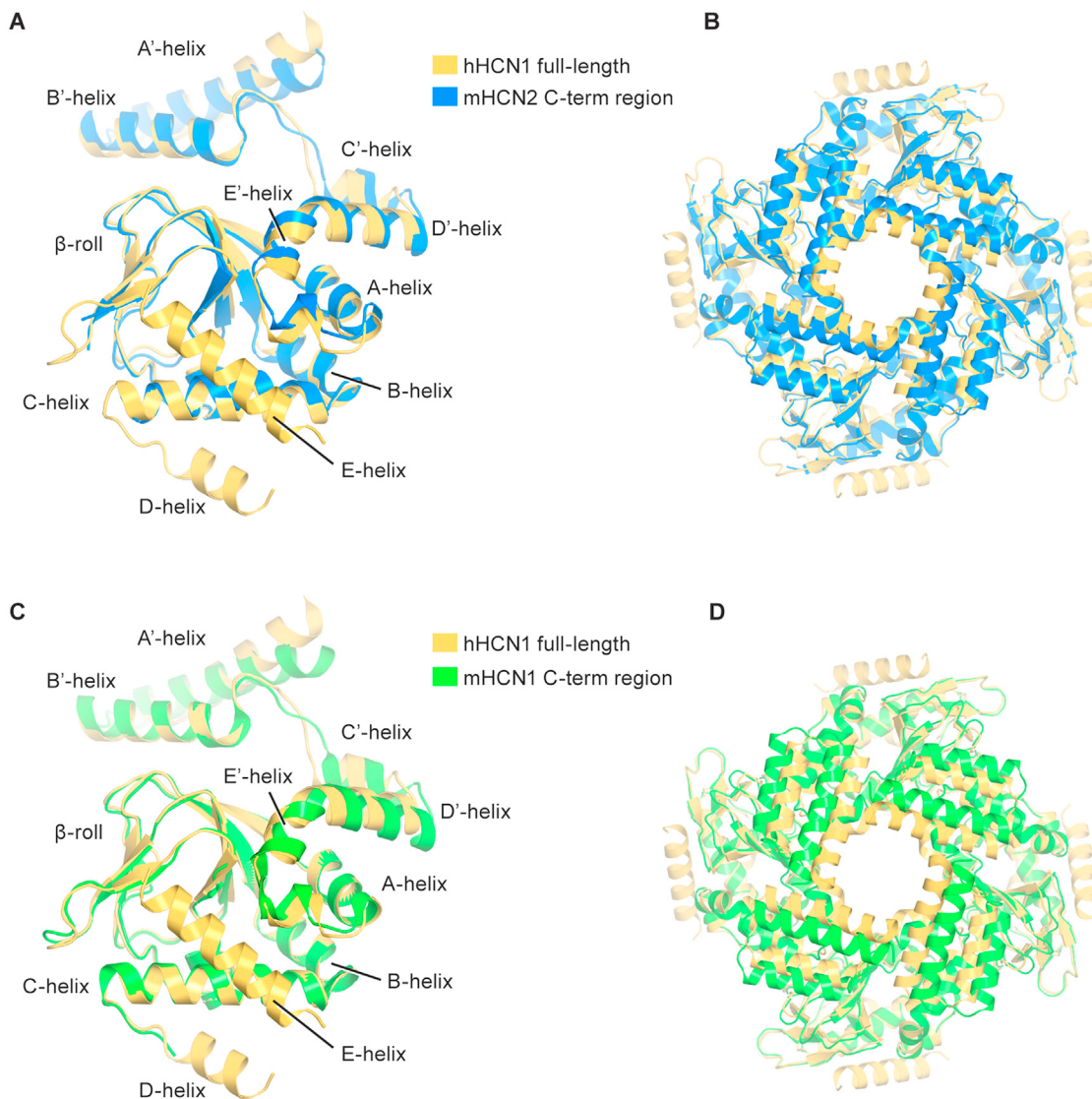


Figure S7. Comparison of C-linkers and CNBDs in the Cryo-EM and Crystal Structures, Related to Figures 6 and 7

(A and C) Superposition of the cytoplasmic domains (single subunit) from the cAMP-bound cryo-EM structure (yellow) and from crystal structures of isolated domains (blue and green) (mHCN2, PDB ID: 1Q43; mHCN1, PDB ID: 3U0Z). The CNBDs align well, whereas the C-linker regions have larger displacements. D- and E-helices of the CNBD are absent in the crystal structures.

(B and D) Superposition of the cytoplasmic tetramers based on C α atoms of β -jelly rolls, in the same view as Figure 7D. The C-terminal fragments of mHCN form a tetramer in the crystal, which creates a larger vestibule than the corresponding region of hHCN1. This is perhaps due to lack of constraints from the transmembrane domains in crystal structures of isolated domains.